catalysts

MDPI

Article

From Powder to Cementitious Matrix: Correlating Physico-Chemical Properties of Photocatalysts with NOx Abatement and Self-Cleaning Performance of Cement Mortars

Wioletta Jackiewicz-Rek [1], Karol Chilmon [1], Maciej Kalinowski [1,*], Beata Jaworska [1] and Filip Chyliński [2]

[1] Faculty of Civil Engineering, Warsaw University of Technology, al. Armii Ludowej 16, 00-637 Warsaw, Poland; wioletta.rek@pw.edu.pl (W.J.-R.); karol.chilmon@pw.edu.pl (K.C.); beata.jaworska@pw.edu.pl (B.J.)
[2] Building Research Institute, Filtrowa 1, 00-611 Warsaw, Poland; f.chylinski@itb.pl
* Correspondence: maciej.kalinowski@pw.edu.pl

Abstract

The photocatalytic performance of TiO_2 powders is commonly associated with specific surface area, crystallite size, and phase composition; however, the extent to which these characteristics remain relevant after incorporation into cementitious materials is not well established. This study investigated nine commercial TiO_2 photocatalysts spanning BET surface areas of 53.8–360.6 m^2/g. The powders were physicochemically characterized and evaluated for NOx abatement, after which seven representative photocatalysts were incorporated into cement mortars at dosages of 4–18 kg/m^3 and tested for NOx removal and self-cleaning performance. At the powder scale, NO removal generally increased with BET surface area, although the improvement diminished above approximately 200–240 m^2/g. Incorporation into mortar fundamentally altered this relationship. P25, despite having the lowest BET surface area and powder-scale NO removal, exhibited the highest mortar-scale activity, exceeding 220 $\mu g/(m^2 \cdot h)$, whereas high-BET photocatalysts generally remained below 80 $\mu g/(m^2 \cdot h)$. DLS and SEM/EDS analyses indicated that composite-scale performance was more closely associated with photocatalyst accessibility after hydration than with nominal powder surface area or agglomerate size alone. Two complementary indicators were therefore introduced: the Photocatalytic Utility Index (PUI), quantifying overall powder-to-composite performance transfer, and the Dose–Response Index (DRI), quantifying response to increasing photocatalyst content. Low-BET photocatalysts exhibited substantially higher PUI and DRI values than high-BET materials.

Keywords: titanium dioxide; cement matrix; cement composites; photocatalytic powders; photocatalysis; NO removal

Check for updates

Academic Editor: Luis Sánchez Granados

Received: 28 October 2026
Revised: 13 November 2026
Accepted: 15 November 2026
Published: 18 November 2026

Copyright: © 2026 by the authors. Licensee MDPI, Basel, Switzerland. This article is an open access article distributed under the terms and conditions of the Creative Commons Attribution (CC BY) license.

1. Introduction

Photocatalytic cementitious composites have been extensively investigated as multifunctional building materials capable of reducing atmospheric pollutants and limiting surface soiling under solar or artificial irradiation [1–3]. Titanium dioxide remains the most widely used photocatalyst in this field because of its chemical stability, availability, and ability to oxidize nitrogen oxides and organic contaminants under UV irradiation. The photocatalytic performance of cement-based materials is governed by several interacting factors, including photocatalyst dosage [4], phase composition, particle size, specific surface area, dispersion state, matrix porosity, pollutant concentration, relative humidity, gas flow rate, and irradiance [5–11]. Besides TiO_2, other inorganic semiconductors, including

zinc oxide (ZnO), tungsten trioxide (WO_3), and bismuth-based compounds, have also been investigated for photocatalytic NOx removal. Nevertheless, TiO_2 remains particularly relevant for cementitious applications due to its established use and compatibility with conventional construction materials.

Incorporation into a cementitious matrix introduces constraints that are absent when photocatalysts are tested as free powders. Photocatalyst particles may become embedded within hydration products [12] or partially shielded by the cement matrix, while their exposure to irradiation and gaseous reactants is additionally affected by surface morphology and pore structure [3,4,13]. Consequently, high photocatalytic activity measured in a powder does not necessarily translate into correspondingly high performance when incorporated into a cementitious composite.

This raises a practical question regarding the value of advanced photocatalyst modification strategies for cement-based applications. Considerable effort is devoted to reducing particle and crystallite dimensions, increasing specific surface area, improving dispersion, or introducing dopants to enhance powder-level photocatalytic activity. Such modifications may require additional grinding, synthesis, or surface treatment procedures, thereby increasing processing complexity, energy consumption, and cost. For example, high-energy ball milling can substantially reduce crystallite size and increase BET surface area but may require processing times of up to 16 h [14]. Whether the resulting improvement in powder properties translates into a proportional benefit after incorporation into cementitious materials remains less clear.

Previous research on this transition has focused predominantly on photocatalyst dispersion, including ultrasonication, high-shear mixing, PCE-based dispersion, mineral carriers, and hybrid carrier–TiO_2 systems designed to reduce agglomeration and improve photocatalyst exposure [9,11]. Comparatively less attention has been devoted to systematically relating the physicochemical properties and photocatalytic activity of the initial powders to the performance of the corresponding cementitious composites.

Particle size represents one of the few powder characteristics investigated systematically in this context. Folli et al., (2012) [15] demonstrated that the relationship between incorporation and photocatalytic performance is not straightforward. Despite the higher BET surface area of nanosized TiO_2, larger particles exhibited superior Rhodamine B degradation, whereas smaller particles were more effective for NOx oxidation. These differences were attributed to the agglomerate structures formed in highly alkaline cement pore solutions. More recently, Akbulut [16] compared TiO_2 particles of 15–35 and 55–75 nm and reported improved photocatalytic activity and pore refinement for the smaller particles. However, systematic comparisons that encompass a broader range of commercial photocatalysts and simultaneously consider their phase composition, specific surface area, particle characteristics, optical properties, and powder-level photocatalytic activity remain scarce.

This knowledge gap is particularly relevant to practical applications, where photocatalysts are commonly introduced during conventional mixing as dry powders or dispersions without complex post-processing. Material selection, therefore, requires understanding not only which photocatalysts perform well in their initial powder form, but also which characteristics are associated with effective photocatalytic performance after incorporation into a cementitious matrix.

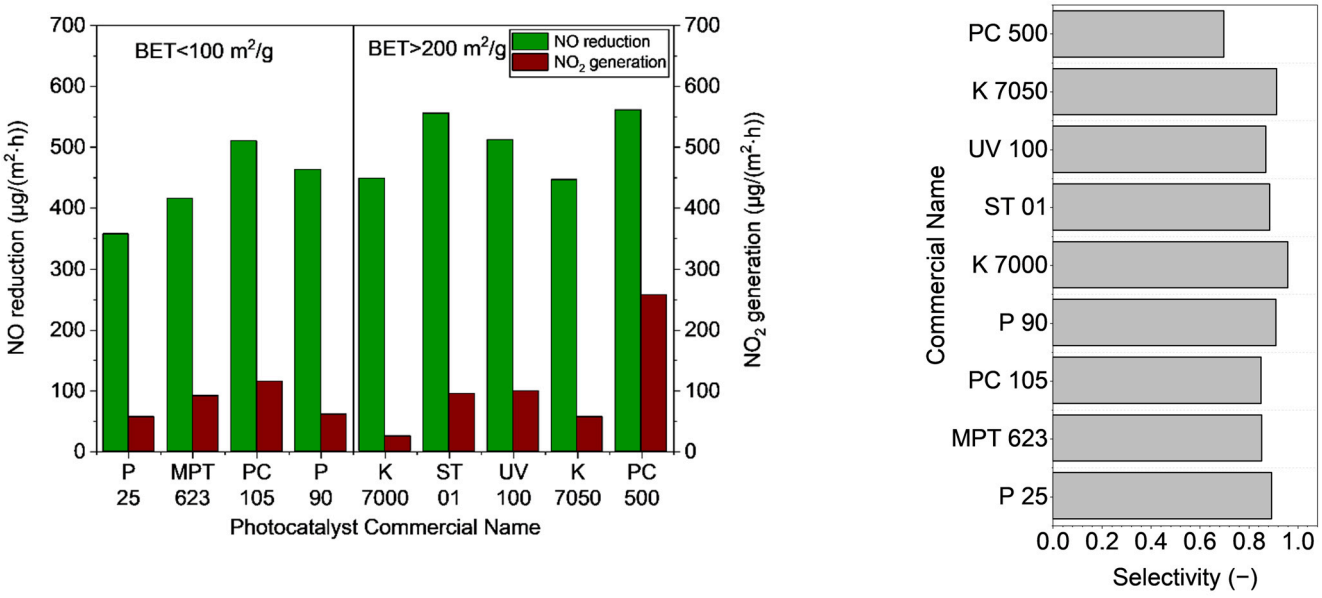
To address this question, nine commercially available TiO_2 photocatalysts were characterized in powder form using XRD, BET, XRF, SEM, UV–Vis spectroscopy, and gas-phase pollutant removal tests. A representative subset was subsequently incorporated into cement mortars and evaluated for NOx abatement and self-cleaning performance. By directly relating powder characteristics and powder-level photocatalytic activity to the performance of the corresponding mortars, the study aimed to identify which powder characteristics

translate into effective photocatalytic performance after incorporation, how this performance responds to increasing photocatalyst content, and to what extent the photocatalytic potential observed in the powder state is utilized in the cementitious composite.

2. Results

2.1. NOx Abatement Performance of Powder Photocatalysts

The NOx abatement tests showed measurable differences in the photocatalytic performance of the investigated powder photocatalysts (Figure 1a). The NO removal rates ranged from 357 to 561 μg/(m²·h), corresponding to approximately a 57% difference between the least and most active samples. The lowest activity was recorded for P25, whereas the highest NO removal rates were obtained for PC500 and ST01. Most photocatalysts exhibited intermediate performance, with NO removal rates generally ranging from 440 to 520 μg/(m²·h). Despite substantial differences in crystal structure, crystallite size, specific surface area, and optical properties, the observed differences in photocatalytic activity remained relatively moderate.



(**a**) (**b**)

Figure 1. Photocatalytic NOx abatement performance of the investigated powder photocatalysts under UV-A irradiation. (**a**) NO removal and NO_2 generation rates expressed as μg/(m²·h); (**b**) Photocatalytic selectivity is calculated as one minus the ratio of NO_2 generated (μmol/(m²·h)) to NO removed (μmol(m²·h)). A value approaching 1 indicates ideal selectivity, where NO is fully oxidized with negligible NO_2 release. Photocatalysts are arranged in ascending order of BET specific surface area.

Considerable differences were also observed in the NO_2 generation rates (Figure 1a). The amount of NO_2 formed during photocatalytic oxidation ranged from 24 to 257 μg/(m²·h). The lowest NO_2 generation was recorded for K7000, whereas PC500 exhibited substantially higher NO_2 formation than all other investigated photocatalysts. Most materials generated NO_2 within a relatively narrow range of approximately 55–115 μg/(m²·h). Interestingly, the ranking of photocatalysts based on NO_2 generation differed from that observed for NO removal. While PC500 achieved the highest NO removal rate, it also produced the largest amount of NO_2. In contrast, K7000 combined relatively high NO removal performance with exceptionally low NO_2 generation.

The calculated photocatalytic selectivity values ranged from 0.70 to 0.96 (Figure 1b). K7000 exhibited the highest selectivity (0.96), whereas PC500 showed the lowest value (0.70). Most photocatalysts achieved selectivity values above 0.85, indicating relatively limited accumulation of NO_2 during photocatalytic oxidation. Although substantial differences were observed in both NO removal and NO_2 generation rates, the variability in selectivity was considerably lower. As a result, the ranking of photocatalysts based on selectivity differed from that obtained using NO removal performance alone.

2.2. Photocatalytic NOx Abatement Performance of Mortar Specimens

The photocatalytic NO removal performance of mortar specimens under UV-A irradiation varied substantially depending on the type and dosage of the incorporated photocatalyst (Figure 2a). Among all investigated materials, P25 exhibited the highest activity, with NO removal increasing from approximately 50–65 $\mu g/(m^2 \cdot h)$ at 4 kg/m^3 to more than 220 $\mu g/(m^2 \cdot h)$ at 18 kg/m^3. A similarly pronounced dosage-dependent increase was observed for P90 and MPT623, although their maximum NO removal rates remained lower than those achieved by P25. In contrast, K7000, UV100, K7050, and ST01 exhibited considerably lower activity across the investigated dosage range, with NO removal rates generally remaining below 80 $\mu g/(m^2 \cdot h)$.

The NO_2 generation rates under UV-A irradiation also differed considerably between the investigated mortar series (Figure 2b). The highest NO_2 generation values were observed for P25 and MPT623. For P25, NO_2 generation increased from approximately 50–80 $\mu g/(m^2 \cdot h)$ at low dosages to values exceeding 100 $\mu g/(m^2 \cdot h)$ at intermediate dosages (8–16 kg/m^3), followed by a decrease at 18 kg/m^3. MPT623 exhibited the highest NO_2 generation rates at dosages between 6 and 10 kg/m^3, reaching up to approximately 170 $\mu g/(m^2 \cdot h)$. However, a pronounced reduction in NO_2 generation was observed at dosages of 12 kg/m^3 or higher, with values generally remaining below 80 $\mu g/(m^2 \cdot h)$. P90 showed intermediate NO_2 generation rates, typically ranging from approximately 30 to 80 $\mu g/(m^2 \cdot h)$. In contrast, K7000, UV100, K7050, and ST01 generated substantially lower NO_2 levels, generally below 40 $\mu g/(m^2 \cdot h)$ across the investigated dosage range.

A comparison of Figure 2a,b revealed two distinct trends in the relationship between NO removal and NO_2 generation. The first group, represented by P25 and MPT623, exhibited relatively high NO_2 generation rates at low and intermediate photocatalyst dosages (up to approximately 10 kg/m^3). Above this threshold, further increases in dosage led to a disproportionate increase in NO removal relative to NO_2 generation. Consequently, the NO_2 generation-to-NO removal ratio progressively decreased with increasing photocatalyst content. This trend was particularly evident for P25 and became even more pronounced for MPT623 at dosages of 12 kg/m^3 and above, where substantial increases in NO removal were accompanied by markedly lower NO_2 generation rates. In contrast, the second group, comprising P90, K7000, K7050, ST01, and UV100, exhibited a relatively stable relationship between NO removal and NO_2 generation across the investigated dosage range, with changes in photocatalyst content producing proportional changes in both parameters.

Photocatalysts with high BET surface areas (>200 m^2/g), including K7000, UV100, K7050, and ST01, generally exhibited a more proportional relationship between NO removal and NO_2 generation over the investigated dosage range. For these materials, increases in photocatalyst dosage resulted in simultaneous increases in both parameters. P90 exhibited an intermediate behavior, combining relatively high NO removal rates with NO_2 generation levels substantially lower than those observed for P25 and MPT623 at comparable dosages.

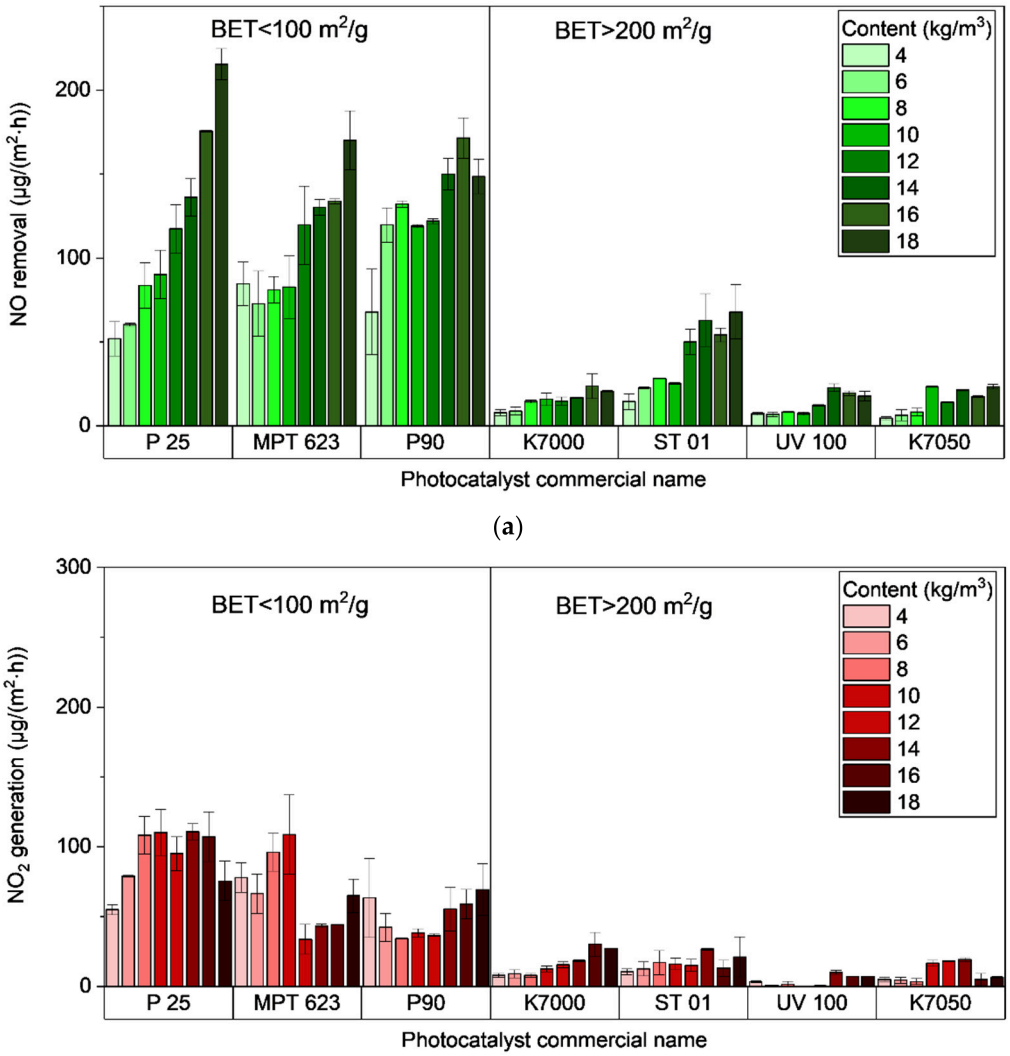
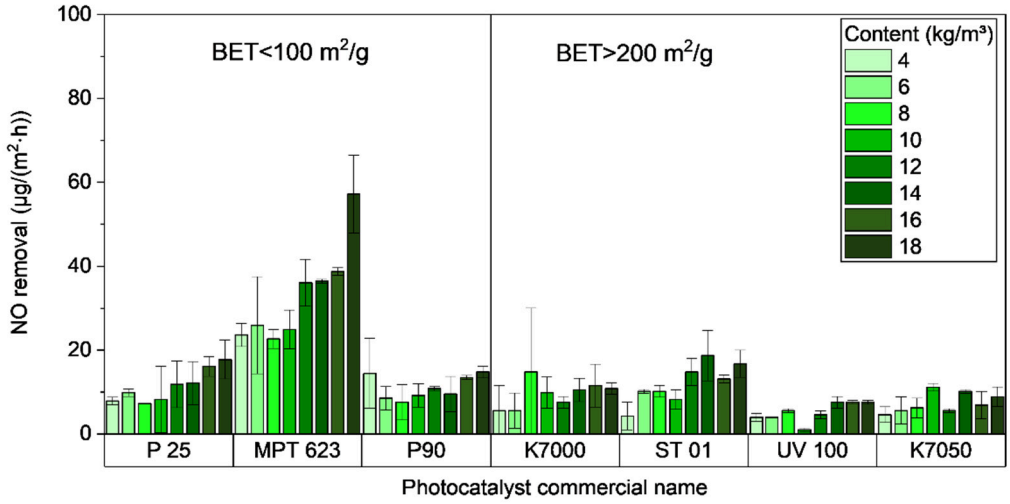


Figure 2. Photocatalytic (**a**) NO removal and (**b**) NO_2 generation rates of mortar specimens incorporating different photocatalysts and photocatalyst dosages under UV-A. Error bars represent standard deviations obtained from two samples.

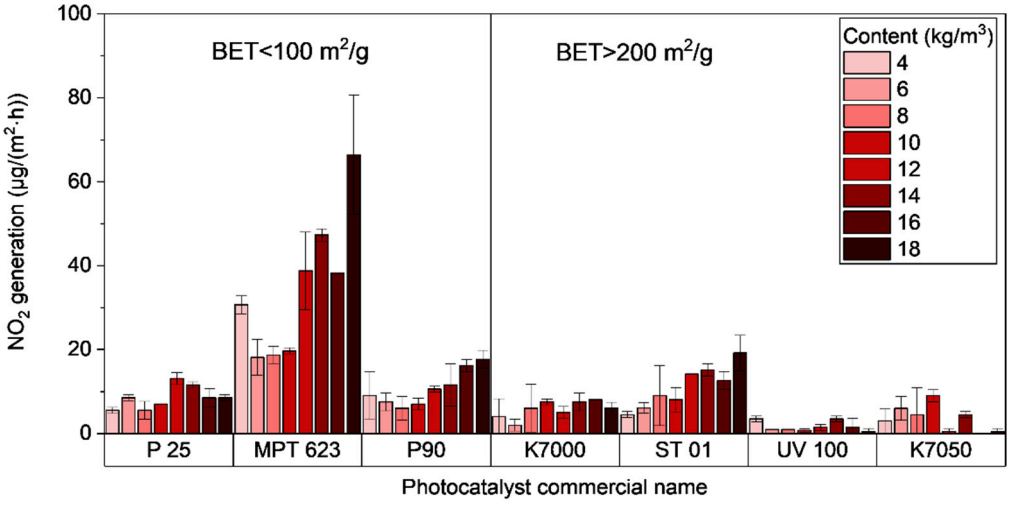
Under visible-light irradiation, all investigated mortars exhibited substantially lower photocatalytic activity than under UV-A irradiation (Figure 3a). Most photocatalysts achieved NO removal rates below 25 $\mu g/(m^2 \cdot h)$ throughout the investigated dosage range. The only notable exception was MPT623, which exhibited a pronounced dose-dependent increase in activity, reaching an NO removal rate of approximately 64 $\mu g/(m^2 \cdot h)$ at 18 kg/m^3. The remaining photocatalysts, including P25, P90, K7050, ST01, K7000, and UV100, showed comparatively limited visible-light activity, with only moderate increases observed at higher photocatalyst dosages.

The corresponding NO_2 generation rates are presented in Figure 3b. Similar to NO removal, MPT623 produced the highest NO_2 levels under visible-light irradiation, with NO_2 generation increasing from approximately 30–40 $\mu g/(m^2 \cdot h)$ at 4 kg/m^3 to more than 75 $\mu g/(m^2 \cdot h)$ at 18 kg/m^3. P90 and P25 exhibited intermediate NO_2 generation rates, generally below 20 $\mu g/(m^2 \cdot h)$, whereas K7000, K7050, ST01, and UV100 produced only minor amounts of NO_2, typically below 10 $\mu g/(m^2 \cdot h)$. Comparison of Figure 3a,b indicates that MPT623 was the only photocatalyst exhibiting a substantial visible-light response. In contrast, K7000, despite being classified as a visible-light-active photocatalyst, demon-

strated photocatalytic performance comparable to that of the conventional photocatalysts investigated in this study.



(**a**)



(**b**)

Figure 3. Photocatalytic (**a**) NO removal and (**b**) NO_2 generation rates of mortar specimens incorporating different photocatalysts and photocatalyst dosages under visible light. Error bars represent standard deviations obtained from two samples.

2.3. Rhodamine B Self-Cleaning Performance of Photocatalytic Mortars

In general, the self-cleaning efficiency (Figure 4) increased with increasing photocatalyst dosage, although the magnitude of this effect varied considerably between the investigated materials. P25 exhibited the highest photocatalytic activity, with R24 values increasing from 0.62 at 4 kg/m^3 to a maximum of 0.98 at 16 kg/m^3. Relatively high self-cleaning efficiencies were also observed for MPT623, P90, and K7000, with maximum R24 values of 0.79, 0.76, and 0.78, respectively. In contrast, ST01 and UV100 exhibited substantially lower activity over the entire dosage range, with maximum R24 values remaining below 0.40.

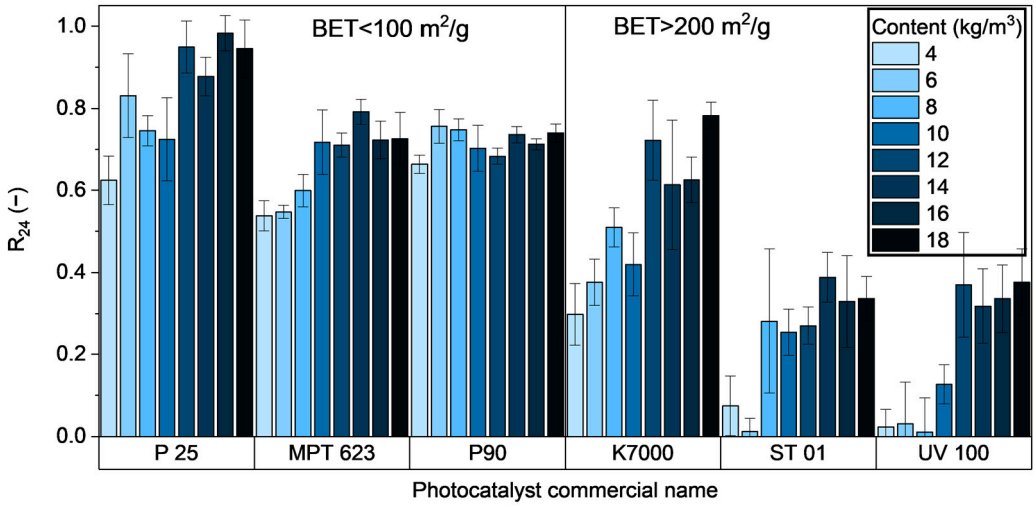


Figure 4. Effect of photocatalyst dosage on Rhodamine B self-cleaning efficiency (R24) after 24 h of UV-A irradiation. Error bars indicate standard deviations calculated from 24 individual measurements obtained from two replicate specimens.

The effect of photocatalyst dosage was most pronounced for P25, where the self-cleaning efficiency increased by more than 50% from the lowest to the highest dosage investigated. A similar but less pronounced trend was observed for MPT623 and K7000. For P90, the self-cleaning efficiency remained relatively stable at dosages above 6 kg/m^3, fluctuating within a narrow range of 0.68–0.76. The lowest efficiencies were observed for UV100 and ST01 at low photocatalyst dosages, with R24 values close to zero.

Variabilities of Rhodamine B tests were generally higher than those observed in the NOx abatement tests. Standard deviations within groups ranged from 0.01 to 0.18, with the largest values recorded for ST01, UV100, and K7000. In contrast, P25, P90, and MPT623 typically exhibited lower standard deviations, most often below 0.06. Overall, the relative scatter in Rhodamine B tests increased for photocatalysts with lower self-cleaning efficiencies.

3. Discussion

Establishing direct relationships between photocatalyst characteristics and photocatalytic performance, whether in powder form or after incorporation into cementitious composites, remains challenging because several physicochemical properties are inherently interrelated. For example, reductions in crystallite size are often accompanied by increases in specific surface area, while changes in crystal structure may simultaneously affect optical properties and charge-carrier dynamics. Consequently, interpreting photocatalytic activity based solely on individual material parameters requires careful consideration of their mutual interactions.

The complexity of those relationships increases further after the incorporation of photocatalysts into cementitious matrices. Unlike photocatalyst powders, whose physicochemical properties can be directly characterized, photocatalyst particles dispersed in fresh cementitious medium are immediately exposed to highly alkaline pore solutions and interactions with cement particles and chemical admixtures. As a result, phenomena such as particle agglomeration, flocculation, electrostatic interactions, and adsorption on cement grains may substantially modify the initial dispersion state of the photocatalyst. Furthermore, the progressive formation of hydration products alters the composite's microstructure, creating a complex pore network while simultaneously embedding or partially covering photocatalyst particles. Consequently, the relationships between the original physicochemical properties of photocatalysts and the measured photocatalytic performance of cementitious compos-

ites are expected to be significantly more complex than those observed for photocatalyst powders alone.

3.1. Physicochemical Properties Versus Photocatalytic Activity of Powder Photocatalysts

The correlation analysis of photocatalyst powders revealed that only two physicochemical parameters were statistically significant predictors of photocatalytic activity (Figure 5). The strongest positive correlations with NO removal were observed for the anatase content ($\rho = 0.68$, $p < 0.05$) and BET specific surface area ($\rho = 0.67$, $p < 0.05$), indicating that photocatalysts characterized by higher surface areas and larger fractions of the anatase phase generally achieved higher NO removal rates. Crystallite size exhibited a moderate negative correlation with NO removal ($\rho = -0.56$), although this relationship was not statistically significant. The exceptionally strong negative correlation between BET surface area and crystallite size ($\rho = -0.97$, $p < 0.05$) confirms that both parameters were closely coupled within the investigated set of photocatalysts and should therefore not be interpreted independently. In contrast, neither band-gap energy nor the maximum absorption wavelength exhibited statistically significant correlations with photocatalytic performance. Similarly, NO_2 generation showed only weak-to-moderate associations with the investigated physicochemical properties, suggesting that the factors governing the overall oxidation rate of NO may differ from those controlling the accumulation of the intermediate NO_2 species.



Figure 5. Spearman (ρ) correlation matrix describing the relationships between the physicochemical properties of the investigated photocatalysts and their photocatalytic performance in powder form. The color scale represents the magnitude and direction of the correlation coefficient, with red indicating positive correlations and blue indicating negative correlations. Cells outlined in red and blue correspond to statistically significant positive and negative correlations, respectively ($p < 0.05$).

Although the anatase content exhibited a statistically significant correlation with NO removal, it was not included in the subsequent regression analysis. This decision was motivated by the highly uneven distribution of anatase content within the investigated dataset, in which most photocatalysts consisted of 100 wt.% anatase, while only a limited number of materials contained substantial rutile fractions. Under such conditions, the observed correlation may primarily reflect the separation between a small number of distinct

groups rather than a continuous physicochemical relationship. In effect, the BET specific surface area was selected as the most suitable parameter for further regression analysis.

Linear regression analysis (Figure 6) yielded a coefficient of determination of $R^2 = 0.415$, indicating that approximately 42% of the observed variability in NO removal could be explained by differences in BET surface area. Nevertheless, ANOVA analysis of the regression model yielded a *p*-value of 0.061, indicating that the observed relationship did not reach statistical significance at the 95% confidence level.

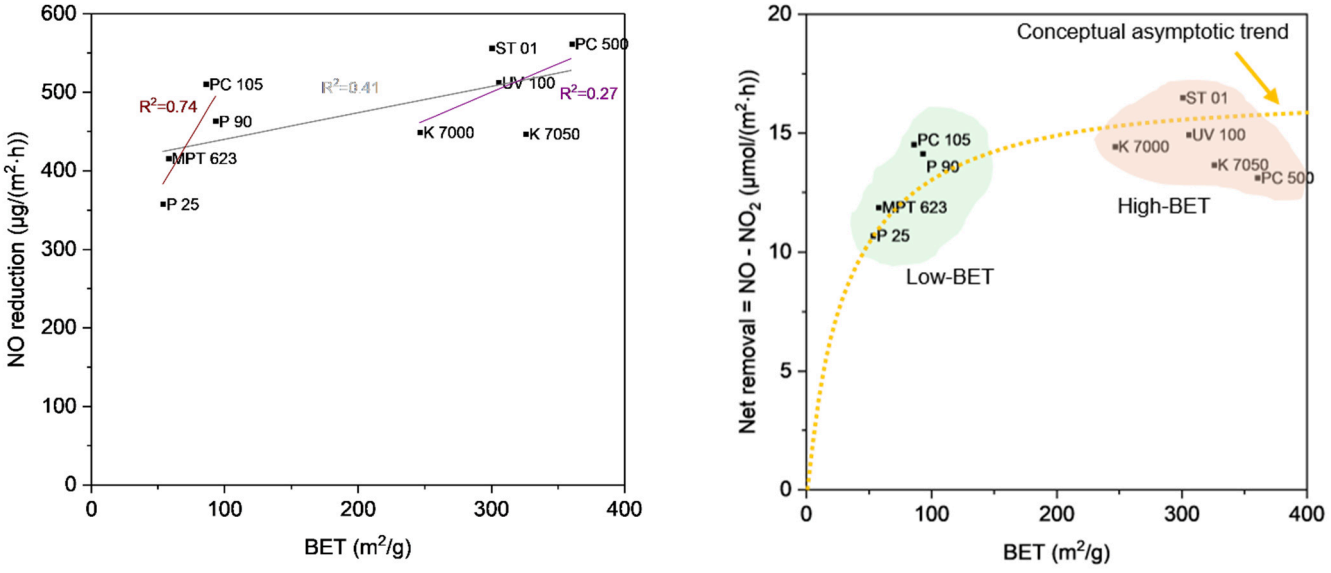


Figure 6. Relationship between BET surface area and (**a**) NO removal (**b**) net removal (ΔNOx) determined for photocatalyst powders.

A closer inspection of the dataset revealed two distinct groups of photocatalysts with different sensitivities of photocatalytic activity to increases in BET surface area. Photocatalysts with relatively low specific surface areas (<100 m^2/g) generally exhibited lower photocatalytic activity, with P25 and MPT623 showing the lowest NO removal rates among the investigated materials. Within this range, increasing BET was accompanied by a pronounced increase in photocatalytic performance, indicating that surface development may be an important factor governing NO abatement in photocatalysts with relatively low surface areas. However, this trend became substantially less pronounced for photocatalysts exhibiting BET values above approximately 240 m^2/g. Although materials such as ST01, UV100, K7050, and PC500 had specific surface areas exceeding 300 m^2/g, the corresponding increase in NO removal performance was relatively modest compared with the differences in BET surface area.

One possible explanation for the diminishing influence of BET surface area at higher BET values has recently been proposed by Naniwa et al. [17] and further generalized by Nandal and Seki [18]. Both studies demonstrated that the photocatalytic activity of TiO_2 powders cannot be interpreted solely on the basis of the total specific surface area, because additional physicochemical processes become increasingly important as particle size decreases. In particular, increasing BET surface area is generally accompanied by a reduction in crystallite size and by changes in charge-carrier dynamics, leading to progressively smaller improvements in photocatalytic performance despite substantial increases in total surface area.

Naniwa et al. [17] showed that although increasing BET generally increases the number of available adsorption sites, it simultaneously shortens the lifetime of photogenerated charge carriers due to a higher density of surface defects. Consequently, photocatalytic activity is governed by the combined influence of specific surface area and carrier lifetime rather than by BET alone, leading to a nonlinear dependence of activity on BET. More recently, Nandal and Seki [18] proposed that the apparent influence of BET is largely a manifestation of more fundamental particle-size effects. Their diffusion-based model predicts that photocatalytic activity progressively approaches a reaction-controlled regime as particle dimensions decrease relative to the minority-carrier diffusion length. Under such conditions, further reductions in particle size—and consequently further increases in BET—produce only limited improvements in photocatalytic activity.

The present results closely follow this behavior. Increasing BET from 53.8 to 93.4 m^2/g (P25–P90) resulted in an approximately 30% increase in NO removal, whereas a further increase from 86.2 to 360.6 m^2/g (PC105–PC500) produced only an additional improvement of approximately 10%, despite a more than fourfold increase in BET surface area. This progressive reduction in the effectiveness of additional surface development is therefore consistent with the transition toward a regime in which BET is no longer the dominant factor governing photocatalytic performance. Instead, other parameters related to charge-carrier transport and surface reaction kinetics are expected to become increasingly important.

In contrast to NO removal, NO_2 generation showed no statistically significant correlations with any of the investigated physicochemical properties of the photocatalysts. Instead, the only significant relationship was observed between NO_2 generation and NO removal ($\rho = 0.73$, $p < 0.05$). This observation indicates that the amount of NO_2 released to the gas phase increased primarily as a consequence of increasing overall photocatalytic activity rather than as a direct function of any individual photocatalyst characteristic—photocatalysts exhibiting higher NO oxidation rates generally produced larger amounts of NO_2, regardless of their BET surface area, crystal structure, or optical properties.

For this reason, the net NOx removal (ΔNOx), calculated according to ISO 22197-1 [19] as the difference between the amount of NO removed and the amount of NO_2 additionally detected in the reactor, provides a more comprehensive descriptor of photocatalytic air-purification performance than NO removal alone. Unlike NO removal, which reflects only the initial oxidation step, ΔNOx additionally accounts for the subsequent fate of the generated NO_2, including its further oxidation to nitrate species and/or its retention on the photocatalyst surface, representing the overall efficiency of photocatalytic NOx abatement.

All investigated photocatalysts exhibited positive ΔNOx values (Figure 6b), indicating that the mole-equivalent removal of NO exceeded the amount of NO_2 remaining in the gas phase. Among photocatalysts with BET surface areas below approximately 100 m^2/g, ΔNOx increased markedly with increasing BET, rising from 10.7–11.9 $\mu mol/(m^2 \cdot h)$ for P25 and MPT623 to 14.1–14.5 $\mu mol/(m^2 \cdot h)$ for P90 and PC105. In contrast, most photocatalysts with BET values above approximately 240 m^2/g clustered within a relatively narrow ΔNOx range, indicating a plateau-like response. Although their BET surface areas increased by more than 100 m^2/g, ΔNOx remained within a relatively narrow range of 13.1–16.5 $\mu mol/(m^2 \cdot h)$.

Interestingly, this plateau-like behavior was not observed experimentally by Naniwa et al. [17], despite their investigation including TiO_2 photocatalysts spanning a comparable BET range (approximately 200–300 m^2/g). It should be noted, however, that their study examined the photocatalytic oxidation of gaseous benzene rather than NOx abatement. Within this BET range, they reported substantial differences in photocatalytic activity among photocatalysts with similar specific surface areas, demonstrating that BET alone was insufficient to explain the observed behavior. The asymptotic response proposed in their

work emerged only after incorporating charge-carrier lifetime into the kinetic model via the SBET τ parameter. Since charge-carrier lifetime was not determined in the present study, the origin of the observed plateau-like ΔNOx response cannot be evaluated directly. Nevertheless, the present results indicate that, even for the photocatalytic oxidation of NO, the beneficial effect of increasing BET becomes progressively exhausted within the BET range of commercially available TiO_2 photocatalysts.

3.2. BET Surface Area Versus Photocatalytic Performance of Cementitious Composites

The relationships identified for photocatalyst powders cannot be directly extrapolated to cementitious composites. Although powder-based tests provide information on the intrinsic photocatalytic properties of photocatalysts under controlled conditions, their incorporation into a cementitious matrix introduces additional factors that modify their effective performance. Consequently, correlations observed for dry powders may weaken upon incorporation into cement-based composites, while factors such as particle dispersion, matrix microstructure, and photocatalyst surface accessibility become increasingly important.

Among these factors, the dispersion state of photocatalyst particles appears to play a key role. Upon contact with the highly alkaline cement pore solution, photocatalyst particles undergo electrostatic interactions that promote rapid aggregation and substantially alter their effective particle-size distribution. Dynamic light scattering (DLS) measurements performed in synthetic cement pore solution (Table 1) confirmed extensive aggregation of all investigated photocatalysts. Mean aggregate sizes ranged from approximately 1.9 to 7.4 μm, greatly exceeding the primary crystallite sizes determined by XRD. At the same time, zeta potentials between approximately −4 and +3 mV indicated very limited colloidal stability: photocatalysts dispersed in cement pore solution should not be regarded as isolated nanoparticles but rather as micron-sized agglomerates whose effective dimensions and surface accessibility differ substantially from those of the primary particles.

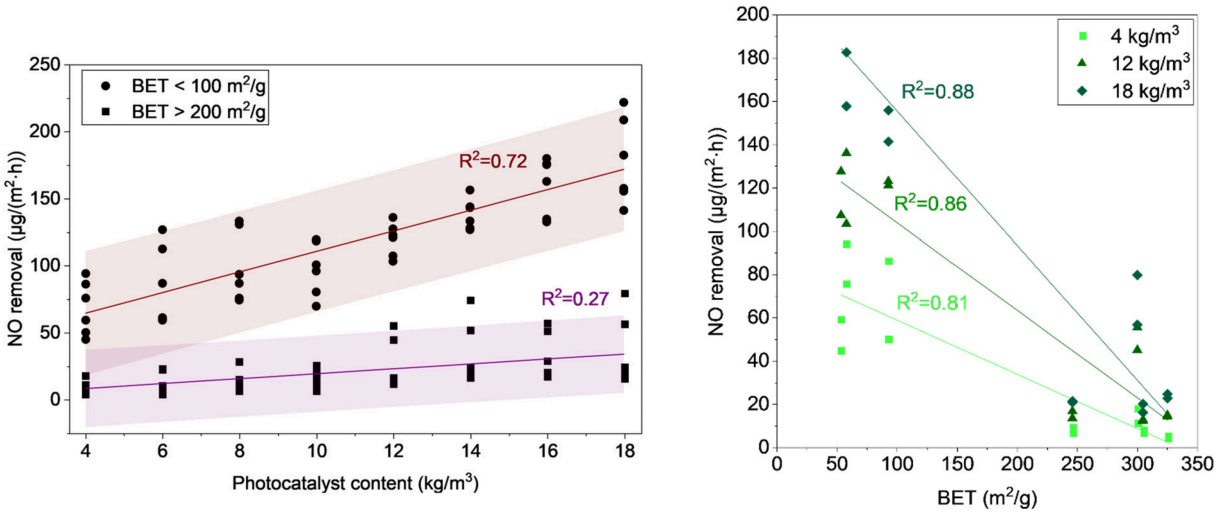
Table 1. Particle size and zeta potential of photocatalyst dispersions measured in synthetic cement pore solution using dynamic light scattering (DLS).

Property	Photocatalyst Commercial Name								
	BET < 100 m^2/g			BET > 200 m^2/g					
	P 25	**MPT 623**	**PC 105**	**P 90**	**K 7000**	**ST 01**	**UV 100**	**K 7050**	**PC 500**
Particle size									
Mean, nm	7418	3853	3821	6035	5154	2980	1945	3599	2080
Minimum, nm	7205	3644	3748	5607	4753	2411	1682	3314	1955
Maximum, nm	7631	4022	3895	6462	5556	3763	2367	3884	2238
Zeta potential, mV	3.044	−4.170	−2.636	−2.266	−3.915	−0.861	1.412	−0.6057	−0.259

Within the aggregated state, no clear separation between the low- and high-BET photocatalysts was observed in terms of agglomerate size. Photocatalysts with BET values exceeding 200 m^2/g generally formed smaller agglomerates than low-BET materials. The largest agglomerates were observed for P25 and P90 (approximately 7.4 and 6.0 μm, respectively), whereas UV100 and PC500 exhibited the smallest average agglomerate sizes (approximately 1.9 and 2.1 μm). Considerable overlap between the two BET groups was evident, with K7000 forming relatively large agglomerates (approximately 5.2 μm) despite its high BET surface area, whereas MPT623, PC105, and K7050 exhibited comparable aggregate sizes. Consequently, the average agglomerate size decreased only moderately, from approximately 5.3 μm for the low-BET photocatalysts to approximately 3.2 μm for

the high-BET group. Therefore, the relatively small differences in agglomerate size alone appear insufficient to explain the pronounced reduction in photocatalytic performance observed for the high-BET photocatalysts.

Despite these relatively modest differences in agglomerate size, the photocatalytic performance of the investigated mortars differed markedly between the two BET ranges. Low-BET photocatalysts exhibited a pronounced increase in NO removal with increasing photocatalyst dosage under UV-A irradiation, indicating that the additional photocatalyst remained effectively accessible for photocatalytic reactions. In contrast, mortars containing photocatalysts with BET values exceeding 200 m^2/g showed only limited response to increasing dosage and maintained relatively low NO removal even at the highest investigated TiO_2 contents (Figure 7a).



(**a**) (**b**)

Figure 7. Relationship between (**a**) mass dosage of photocatalysts investigated in cement mortars (divided into two groups, photocatalyst of BET below 100 m^2/g and above 200 m^2/g), and NO removal performance under UV-A irradiance; (**b**) BET surface area of photocatalysts embedded within cement mortars and their average NO removal performance under UV-A irradiance for minimal, average, and maximal photocatalyst content.

Although regression analyses performed on the complete dataset yielded relatively high coefficients of determination (Figure 7b), particularly for BET surface area, these relationships were primarily driven by the separation of photocatalysts into two distinct behavioral groups rather than by a continuous trend across the entire population. Accordingly, regression analyses were repeated separately for low-BET (<100 m^2/g) and high-BET (>200 m^2/g) photocatalysts. Within either group, no statistically significant relationship between BET surface area and NO removal was observed, except for mortars containing 18 kg/m^3 of photocatalyst. These results indicate that, after incorporation into the cementitious matrix, BET alone is no longer the dominant parameter governing photocatalytic performance.

Previous studies investigating the influence of TiO_2 particle size and BET surface area on the photocatalytic performance of cementitious composites have almost exclusively considered photocatalysts with relatively low specific surface areas, typically below 100 m^2/g. Within this range, higher BET values were consistently associated with improved photocatalytic activity, leading to the generally accepted conclusion that increasing specific surface area enhances NOx abatement in cementitious composites. Chen and Poon [20], for example, compared photocatalysts with BET surface areas of 7.5 and 58.8 m^2/g and reported

superior NOx removal for the higher-BET P25 photocatalyst, attributing this effect to the larger number of accessible reaction sites. They also observed that increasing TiO_2 dosage did not produce a proportional increase in photocatalytic activity, suggesting that photon transport and reactant diffusion within the cement matrix gradually became rate-limiting.

Similarly, Folli et al. [21] compared a nanosized TiO_2 photocatalyst (BET = 78.9 m^2/g) with a microsized material (BET = 8.7 m^2/g) and likewise reported superior NOx degradation for the higher-BET photocatalyst. The authors concluded that the small dimensions of NO molecules (100–200 pm) enabled efficient diffusion to both micro- and nano-sized TiO_2 aggregates, making BET surface area an important parameter governing photocatalytic performance.

More recently, Baudys et al. [22] compared immobilized P25 and P90 photocatalytic layers (BET ≈ 45 and 109 m^2/g, respectively) using gaseous VOC degradation as the performance indicator. Although the higher-BET photocatalyst consistently exhibited superior photocatalytic activity, pollutant conversion increased by only approximately 10–30% despite an approximately 2.4-fold increase in BET surface area. The authors attributed this non-proportional response to the limited accessibility of the TiO_2 surface after immobilization and to restrictions associated with light penetration through the photocatalytic layer.

The present results are fully consistent with these observations within the investigated low-BET range. Increasing BET from 53.8 m^2/g (P25) to 93.4 m^2/g (P90) led to higher NO removal across most photocatalyst dosages, confirming the beneficial effect of increased specific surface area. However, the increase in photocatalytic activity was not proportional to the increase in BET. Depending on TiO_2 dosage, NO removal increased by approximately 30–100%, whereas at higher photocatalyst contents (14–18 kg/m^3) the difference between P25 and P90 became relatively small or disappeared altogether.

Collectively, these observations suggest that the beneficial effect of increasing BET surface area is not unlimited. Since previous studies have rarely investigated photocatalysts with BET values exceeding approximately 200 m^2/g, the existence of an upper BET threshold has remained largely unexplored. The present results indicate that the positive BET–activity relationship established for low-BET photocatalysts does not extend indefinitely. Instead, beyond approximately 200 m^2/g, further increases in BET surface area produce only marginal improvements in NO removal despite substantial increases in the nominal surface area of the photocatalyst powder.

A possible explanation is provided by previous studies investigating the interactions between TiO_2 particles and cement hydration products. Folli et al. [21] demonstrated that the highly alkaline cement pore solution and the presence of calcium ions strongly promote TiO_2 aggregation, indicating that the accessibility of photocatalyst particles within cementitious systems cannot be inferred directly from their primary particle size.

Hamidi and Aslani [23] further concluded that the photocatalytic activity of cementitious composites is governed primarily by the fraction of photocatalytically accessible TiO_2 surface rather than by the nominal BET surface area of the powder. They also highlighted that hydration products may progressively cover TiO_2 particles, reducing the available reaction area, while nano-sized TiO_2 particles may simultaneously serve as preferential nucleation sites for cement hydration products. Similar conclusions were reported by Akbulut [16], who demonstrated that reducing TiO_2 particle size from 55–75 nm to 15–35 nm accelerated cement hydration and promoted matrix densification through enhanced nucleation and microfiller effects.

Collectively, these observations suggest that the internal structure of the agglomerates, rather than their overall hydrodynamic dimensions, governs their interactions with the hydrating cement matrix. Although DLS measurements demonstrated that all investigated photocatalysts formed micron-sized agglomerates and that the differences in agglomerate

size were relatively modest, XRD analysis revealed substantially finer crystallites for the high-BET photocatalysts (8–10 nm) than for the low-BET materials (18–33 nm). Consequently, agglomerates of comparable micrometer dimensions may exhibit markedly different interfacial characteristics. The substantially finer crystallite structure associated with the high-BET photocatalysts is expected to increase the contact area between the agglomerates and the surrounding cement paste, providing more favorable conditions for the nucleation and growth of hydration products directly on the photocatalyst surface.

Consequently, the exceptionally high intrinsic BET surface area of high-BET photocatalysts may not translate into a proportional increase in photocatalytically accessible surface after hardening. Instead, a greater fraction of the photocatalyst surface may become incorporated into or covered by hydration products, thereby reducing the amount of TiO_2 exposed at the mortar surface. This hypothesis was further examined using SEM and EDS observations of the mortar surface (Figure 8).

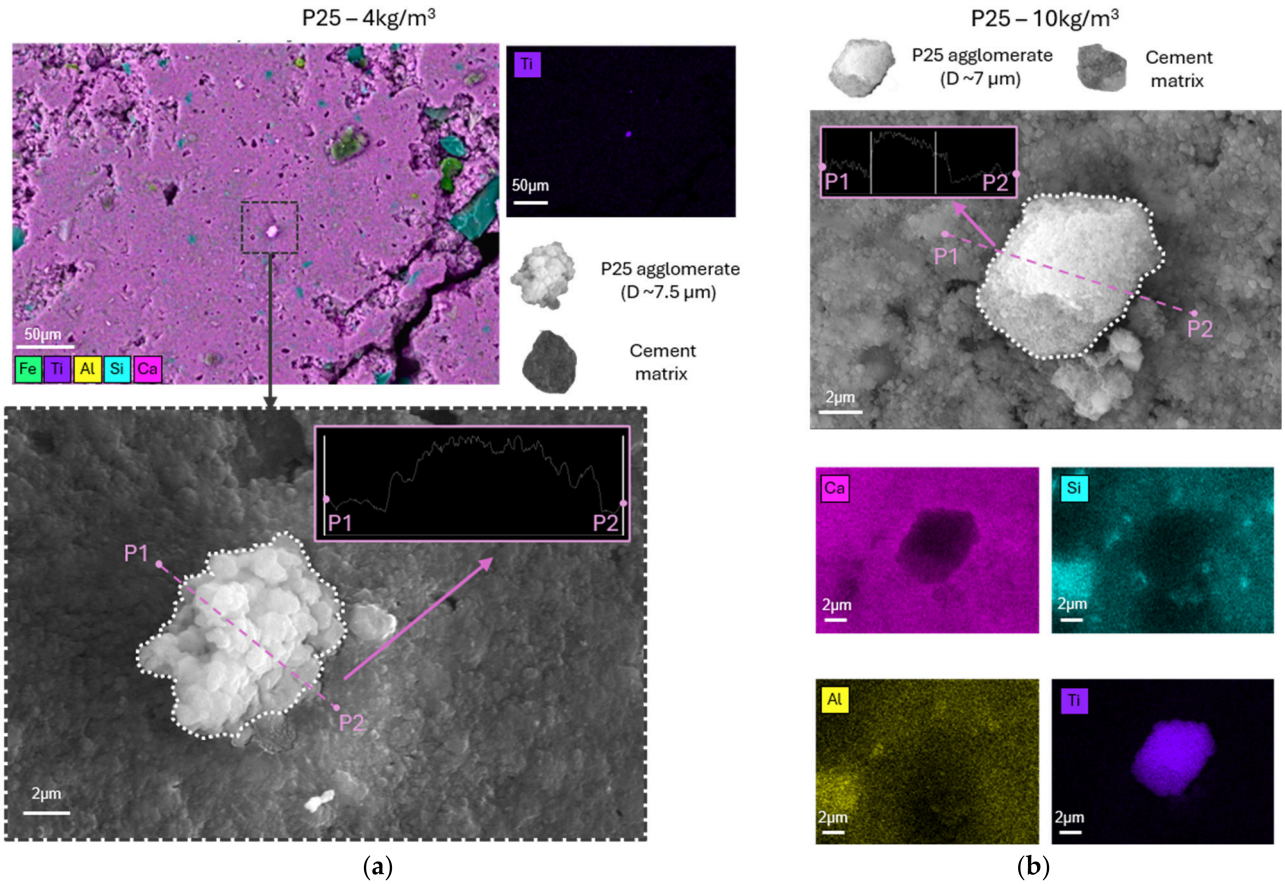


Figure 8. Representative partially exposed TiO_2 agglomerates identified on the surface of mortars containing P25; (**a**) P25 (4 kg/m^3): localization of the agglomerate using an EDS layered image followed by high-magnification SEM imaging. (**b**) P25 (10 kg/m^3): SEM image of a representative surface agglomerate with the corresponding line profile and Ti, Ca, Si, and Al elemental maps. In both cases, the line profiles indicate that the agglomerates protrude above the surrounding cement matrix, while Ti mapping confirms that the exposed features correspond to TiO_2-rich agglomerates.

In mortars containing P25, numerous TiO_2 agglomerates were identified at the composite surface and were accompanied by intense Ti signals in the corresponding EDS maps (Figure 8). The observed agglomerates exhibited characteristic dimensions of approximately 7–7.5 µm, closely matching the average aggregate size determined by DLS (7.4 µm). EDS elemental mapping revealed significant local enrichment in Ti within these protruding features, indicating that they corresponded to TiO_2-rich agglomerates. While several

agglomerates remained partially exposed above the surrounding cement matrix, others appeared partially covered by hydration products, indicating that progressive overgrowth is a natural consequence of cement hydration, even for low-BET photocatalysts. The intensity profiles measured across representative agglomerates were consistent with the presence of protruding surface features associated with the exposed TiO_2 agglomerates.

A different surface morphology was observed for mortars containing K7000 (Figure 9). Similar to P25, Ti-enriched regions embedded within the cement matrix were identified by combining SEM observations with EDS elemental mapping. However, unlike P25, repeated SEM examinations did not show clearly exposed TiO_2 agglomerates protruding above the mortar surface. Instead, the Ti signal was associated predominantly with regions covered by cement hydration products, indicating that the K7000 photocatalyst was incorporated into the near-surface cement matrix to a greater extent than P25. Although the present observations are qualitative and do not permit quantitative determination of the fraction of exposed photocatalyst, they consistently indicate a lower degree of surface exposure for K7000, thereby reducing the amount of photocatalytically accessible TiO_2 at the mortar surface.

The self-cleaning results revealed a markedly different behavior from that observed for NO removal. While K7000 exhibited substantially lower NO removal than the low-BET photocatalysts even at high dosages (>10 kg/m^3), its Rhodamine B degradation efficiency increased markedly with increasing dosage and, above approximately 10 kg/m^3, became comparable to that of P25 and P90 (Figure 4). Thus, the reduced NO removal observed for K7000 was not accompanied by an equally pronounced reduction in self-cleaning performance, suggesting that the relative importance of the processes controlling photocatalytic performance differed between the two tests.

This difference can be considered in relation to the distinct physicochemical conditions governing gaseous NO oxidation and dye photodegradation. In heterogeneous NO oxidation, the reaction depends on the adsorption of gaseous NO and oxygen at illuminated TiO_2 surfaces and on the availability of photogenerated charge carriers and reactive oxygen species. Photogeneration of charge carriers and the subsequent formation of hydroxyl and superoxide radicals can be represented by Equations (1)–(4):

$$TiO_2 + h\nu \rightarrow e^- + h^+ \quad (1)$$

$$h^+ + H_2O_{ads} \rightarrow OH + H^+ \quad (2)$$

$$h^+ + OH^-_{ads} \rightarrow OH \quad (3)$$

$$e^- + O_2 \rightarrow O_2^{\cdot -} \quad (4)$$

These reactive species participate in successive surface reactions leading from NO through NO_2 to nitrate species. Relative humidity (RH) is therefore an important experimental parameter because it affects both surface water availability and competitive adsorption at the photocatalyst surface. Previous studies have reported a non-monotonic dependence of photocatalytic NO removal on relative humidity [24–26]. At low RH, limited surface water availability may restrict hydroxyl radical formation, whereas at higher RH, increased water coverage can compete with NO for adsorption, progressively reducing the availability of surface sites. Accordingly, optimal NO removal has commonly been reported at intermediate RH levels, typically around 30–50%, although the exact range depends on the photocatalyst and experimental configuration.

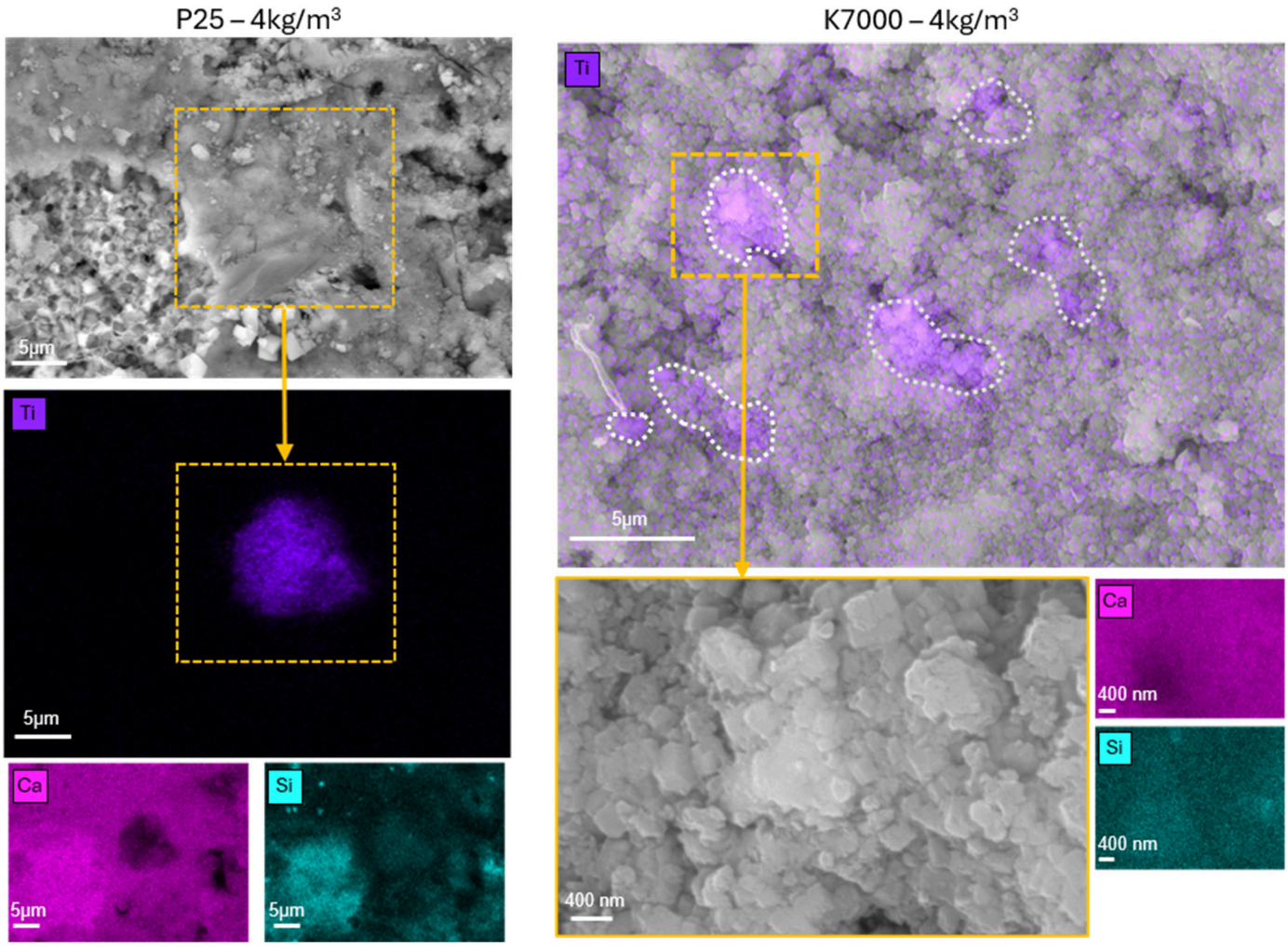


Figure 9. SEM and EDS characterization of TiO_2 agglomerates embedded within the cement matrix. (**a**) P25-containing mortar (4 kg/m^3): SEM image of a TiO_2 agglomerate covered by cement hydration products together with the corresponding Ti, Ca, and Si elemental maps confirming Ti enrichment within the selected region. (**b**) K7000-containing mortar (4 kg/m^3): EDS layered image showing Ti-enriched regions at the mortar surface (dotted outlines) and high-magnification SEM image of a representative Ti-enriched region. The corresponding Ca and Si elemental maps confirm that the Ti-containing region is likewise covered by cement hydration products.

The Rhodamine B test was conducted under substantially different conditions. The dye was deposited directly onto the mortar surface, eliminating gas-phase transport limitations, while the UV-A irradiance was approximately four times higher and the relative humidity was 40–50%, compared with approximately 18% during the NO removal measurements. The higher RH would therefore be expected to increase surface water availability for hydroxyl radical formation relative to the considerably drier conditions in the NO test, while the higher irradiance would increase the rate of photocarrier generation. However, reactive oxygen species concentrations were not measured directly in the present study. Recent ESR and scavenger studies have shown that hydroxyl radicals can play a predominant role in Rhodamine B photodegradation, with superoxide radicals and singlet oxygen providing additional contributions [27].

The behavior of K7000 may additionally be influenced by its carbon modification. Previous studies on carbon-modified TiO_2 have reported suppressed electron–hole recombination, enhanced formation of reactive oxygen species, and increased adsorption

of aromatic organic molecules [27–29]. These effects, investigated using photoluminescence, ESR, scavenger, and adsorption measurements, have been associated with enhanced photodegradation of Rhodamine B and other organic dyes.

These observations in the literature provide one possible explanation for the distinct behavior of K7000, which was the only carbon-modified photocatalyst among the high-BET materials investigated. SEM/EDS observations indicated a lower degree of K7000 exposure at the mortar surface, consistent with its relatively poor performance in gaseous NO removal. However, the different experimental conditions in the Rhodamine B test, together with the previously reported effects of carbon-modified TiO_2, may partly explain why this disadvantage became less pronounced as K7000 dosage increased. This interpretation is consistent with Rhodamine B degradation becoming comparable to that of P25 and P90 above approximately 10 kg/m^3, although neither reactive oxygen species generation nor dye adsorption was measured directly in the present study.

The different relative performances observed in the NO removal and Rhodamine B tests, therefore, suggest that the two methods probe different aspects of photocatalytic performance. They should consequently be regarded as complementary rather than interchangeable when assessing photocatalytic cementitious materials, particularly when photocatalysts with substantially different surface chemistry and behavior after incorporation are compared.

3.3. Retention of Photocatalytic Performance After Incorporation into Cementitious Composites

The extent to which powder-scale photocatalytic performance was transferred to the cementitious matrix was evaluated using two complementary indicators: the Photocatalytic Utility Index (PUI) and the Dose–Response Index (DRI). PUI represents the overall utilization of the mortar's powder-level photocatalytic performance over the investigated photocatalyst content range (Figure 10). It was calculated from the area under the normalized dose–response curve, where the net NOx removal measured for each mortar was normalized to that of the corresponding photocatalyst powder under the same irradiation conditions. Accordingly, PUI approaches 1 when the mortar maintains a net NOx removal rate close to the powder-equivalent reference level throughout the investigated content range, whereas values approaching 0 indicate weak transfer of powder-level performance to the composite.

The Dose–Response Index (DRI) was defined as the slope of the linear approximation of normalized net NOx removal as a function of normalized photocatalyst content, with the investigated content range (4–18 kg/m^3). Consequently, DRI is dimensionless and represents the overall change in relative photocatalytic performance across the investigated photocatalyst content range. PUI and DRI therefore provide complementary information: PUI characterizes the overall level of powder-equivalent performance expressed by the composite, whereas DRI characterizes the extent to which this relative performance increases with photocatalyst content.

The calculated PUI values showed a clear separation between the low- and high-BET photocatalysts. P90 exhibited the highest PUI (0.238), followed by MPT623 and P25 (0.179 and 0.159, respectively). In contrast, PUI values for the high-BET photocatalysts ranged from 0.012 to 0.060. ST01 exhibited the highest value within this group (0.060), whereas K7000, K7050, and UV100 remained below 0.03. Thus, over the investigated photocatalyst content range, the low-BET materials expressed on average approximately 16–24% of their powder-equivalent net NOx removal, compared with only approximately 1–6% for the high-BET materials.

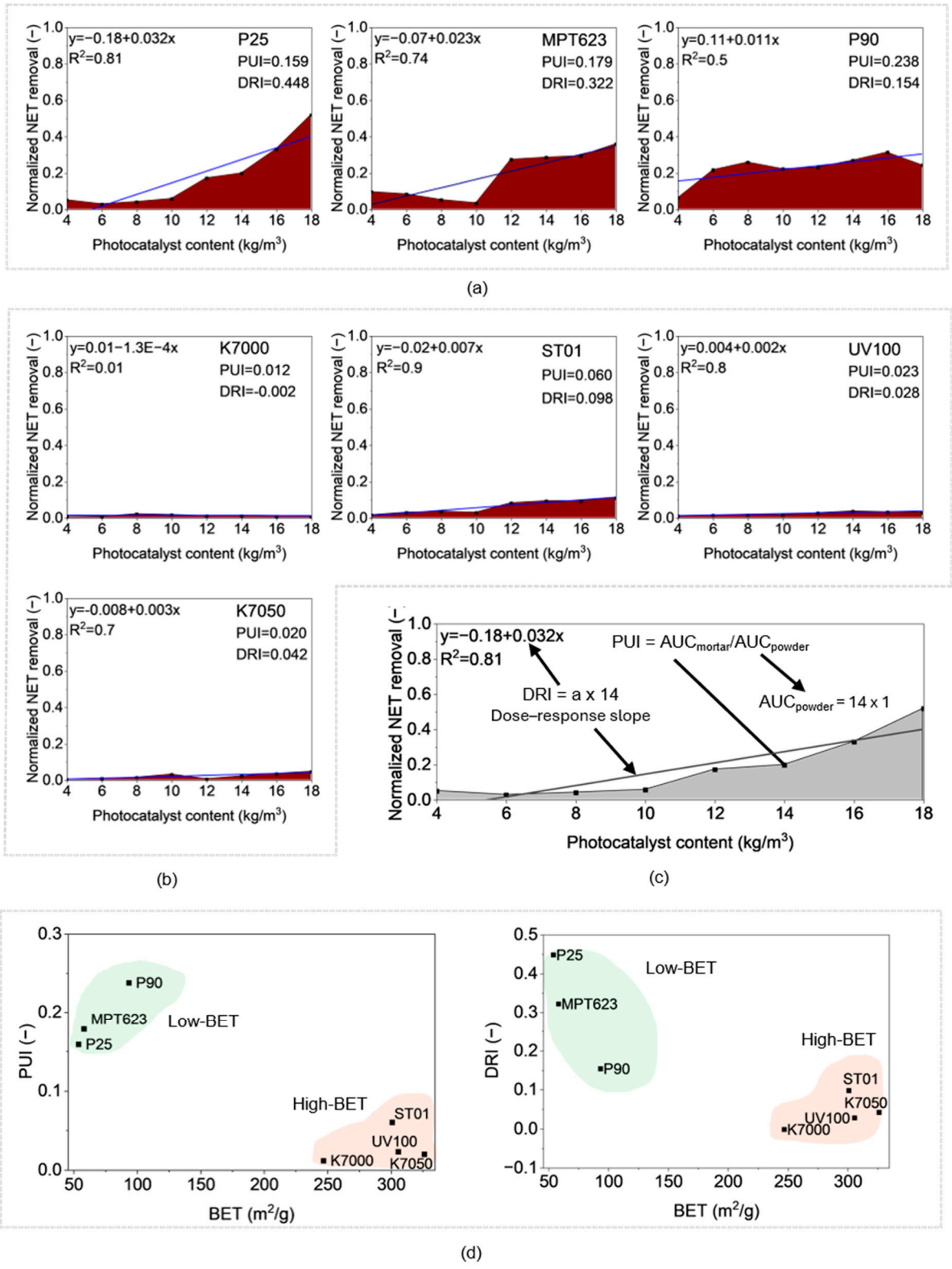


Figure 10. Normalized net NOx removal of photocatalytic mortars investigated in the study as a function of photocatalyst dosage. For each photocatalyst, the normalized value was calculated by dividing the net NOx removal of the modified mortar by the net NOx removal measured for the corresponding photocatalyst powder under the same irradiation condition; (**a**) photocatalytic performance of mortars modified with low-BET photocatalysts; (**b**) photocatalytic performance of mortars modified with high-BET photocatalysts; (**c**) visualization of PUI and DRI calculation method; (**d**) the comparison of PUI and DRI obtained for all investigated powders as a function of BET powder area.

The DRI values provided a complementary distinction. P25 exhibited the strongest dose–response, with a DRI of 0.448, followed by MPT623 (0.322) and P90 (0.154). Considerably lower DRI values were obtained for the high-BET photocatalysts: K7000 showed essentially no systematic response to increasing photocatalyst content (DRI = −0.002), while UV100, K7050, and ST01 exhibited DRI values of 0.028, 0.042, and 0.098, respectively. Thus, within the investigated content range, the low-BET photocatalysts generally exhibited a substantially stronger increase in normalized net NOx removal with increasing photocatalyst content than the high-BET materials. Conversely, the high-BET materials exhibited both low PUI and low DRI, indicating that their low powder-to-composite performance transfer was not substantially compensated by increasing their content within the investigated range. Importantly, the separation observed in Figure 10d should not be interpreted as evidence of a continuous relationship between BET surface area and either index, because photocatalysts with intermediate BET surface areas between 93.4 and 246.8 m^2/g were not represented in the investigated set.

The complementary character of PUI and DRI also provides a potentially useful framework for photocatalyst selection. A material with a high PUI provides relatively high powder-equivalent performance over the investigated content range, whereas a high DRI indicates that increasing its content continues to produce a substantial increase in relative composite performance. Neither parameter alone, therefore, provides a complete criterion for material selection. For example, P90 exhibited the highest PUI but a lower DRI than P25 and MPT623, indicating comparatively high utilization of its powder-level performance but a weaker incremental response to increasing content. P25 showed the opposite tendency, combining a lower PUI with the highest DRI. These differences may become relevant when photocatalyst content is constrained by material cost, rheological effects, mechanical performance, or other technological requirements.

For practical material selection, the two descriptors could therefore be combined into a single application-specific utility index (U). In its simplest normalized form, such an index could be expressed as:

$$U = \omega_{PUI} \cdot PUI + \omega_{DRI} \cdot DRI \quad (5)$$

where PUI and DRI are normalized values and ω_PUI + ω_DRI = 1. Accordingly, changing the relative weights produces a linear variation in (U). At (ω_PUI = 0), the utility value is determined exclusively by DRI, whereas at (ω_PUI = 1), it is determined exclusively by PUI. The minimum and maximum utility values are therefore defined by the smaller and larger of the two normalized indices. A positive slope (for this normalized setup, PUI—DRI) indicates that the utility of a photocatalyst increases as PUI is assigned greater importance. Such a material is favored when consistent utilization of its powder-scale activity across the investigated dosage range is prioritized. A negative slope indicates that utility increases as greater weight is assigned to DRI, thereby identifying photocatalysts whose principal advantage is a pronounced performance improvement with increasing dosage. A slope close to zero indicates that PUI and DRI provide similar assessments, making the calculated utility comparatively insensitive to the selected weights. This approach could subsequently be extended to include additional criteria, including material cost, self-cleaning performance, NO_2 selectivity, or effects on fresh and hardened composite properties. At present, however, it should be regarded as a conceptual framework for multicriteria photocatalyst selection rather than a validated universal index.

The PUI and DRI values obtained here are also specific to the incorporation route and cementitious matrix used in the present study. The photocatalysts were introduced directly as dry powders during mortar mixing, representing the simplest incorporation procedure. Alternative approaches, including pre-dispersion in water, ultrasonication, high-shear dispersion, or the use of mineral carriers, may alter particle distribution and surface

exposure and could therefore result in different PUI and DRI values. In particular, the very low values obtained for the high-BET photocatalysts should not be generalized as evidence that such materials are unsuitable for cementitious applications. Rather, they demonstrate their limited utilization under the direct powder-addition conditions. For highly dispersed nanoscale photocatalysts, dedicated dispersion procedures or carrier-based incorporation may provide substantially different outcomes.

The characteristics of the cementitious matrix constitute a second important boundary condition. The present analysis was performed using a high-performance mortar with relatively low porosity; consequently, the absolute PUI and DRI values cannot be assumed to apply to matrices with substantially different water-to-binder ratios, pore structures, surface roughness, or hydration characteristics. More porous matrices or incorporation strategies that preferentially locate photocatalyst particles near the exposed surface could produce different powder-to-composite relationships. PUI and DRI should therefore be regarded as system-level descriptors of a given photocatalyst–matrix–incorporation combination, rather than intrinsic properties of the photocatalyst itself. Their broader applicability requires validation across different cementitious matrices and incorporation strategies.

4. Materials and Methods

4.1. Materials

4.1.1. Photocatalysts

Nine commercially available titanium dioxide-based photocatalysts intended for photocatalytic and environmental applications were used in the study. The investigated materials included Aeroxide P25 and Aeroxide P90 (Evonik, Essen, Germany), KRONOClean 7000 and KRONOClean 7050 (Kronos TITAN GmbH, Leverkusen, Germany), PC105 and PC500 (Tayca/Toronox, Tokyo, Japan), ST01 and MPT623 (Ishihara Sangyo Kaisha, Osaka, Japan), and UV100 (Venator, Wynyard, UK). The photocatalysts differed in terms of crystalline phase composition, crystallite size, specific surface area, optical properties, and morphology. The results are summarized in Table 2, and representative SEM micrographs are shown in Figure 11. The complete XRD patterns, the corresponding Rietveld refinement plots, and the full UV–Vis absorption spectra of the investigated photocatalysts are provided in the Supplementary Materials [S1–S3].

Table 2. Physicochemical properties of investigated photocatalysts.

ID	Commercial Name	BET Surface	Phase Composition		Crystallite Size		Band-Gap Energy	λ_{max}	Modification
		m^2/g	Anatase	Rutile	Anatase	Rutile	eV	nm	
			%wt	%wt	nm	nm			
PH1	P25	53.8 ± 0.2	87	13	33	54	3.30	297	None
PH2	MPT623	58.1 ± 0.3	–	100	–	28	3.06	308	Pt-loaded
PH3	PC105	86.2 ± 0.2	100	–	30	–	3.30	318	None
PH4	P90	93.4 ± 0.2	91	9	18	32	3.25	306	None
PH5	K7000	246.8 ± 2.9	100	–	10	–	3.29	322	C-doped
PH6	ST01	300.9 ± 1.2	100	–	9	–	3.26	310	None
PH7	UV100	305.7 ± 1.2	100	–	9	–	3.33	314	None
PH8	K7050	326.2 ± 2.6	100	–	8	–	3.31	298	None
PH9	PC500	360.6 ± 1.9	100	–	8	–	3.33	314	None

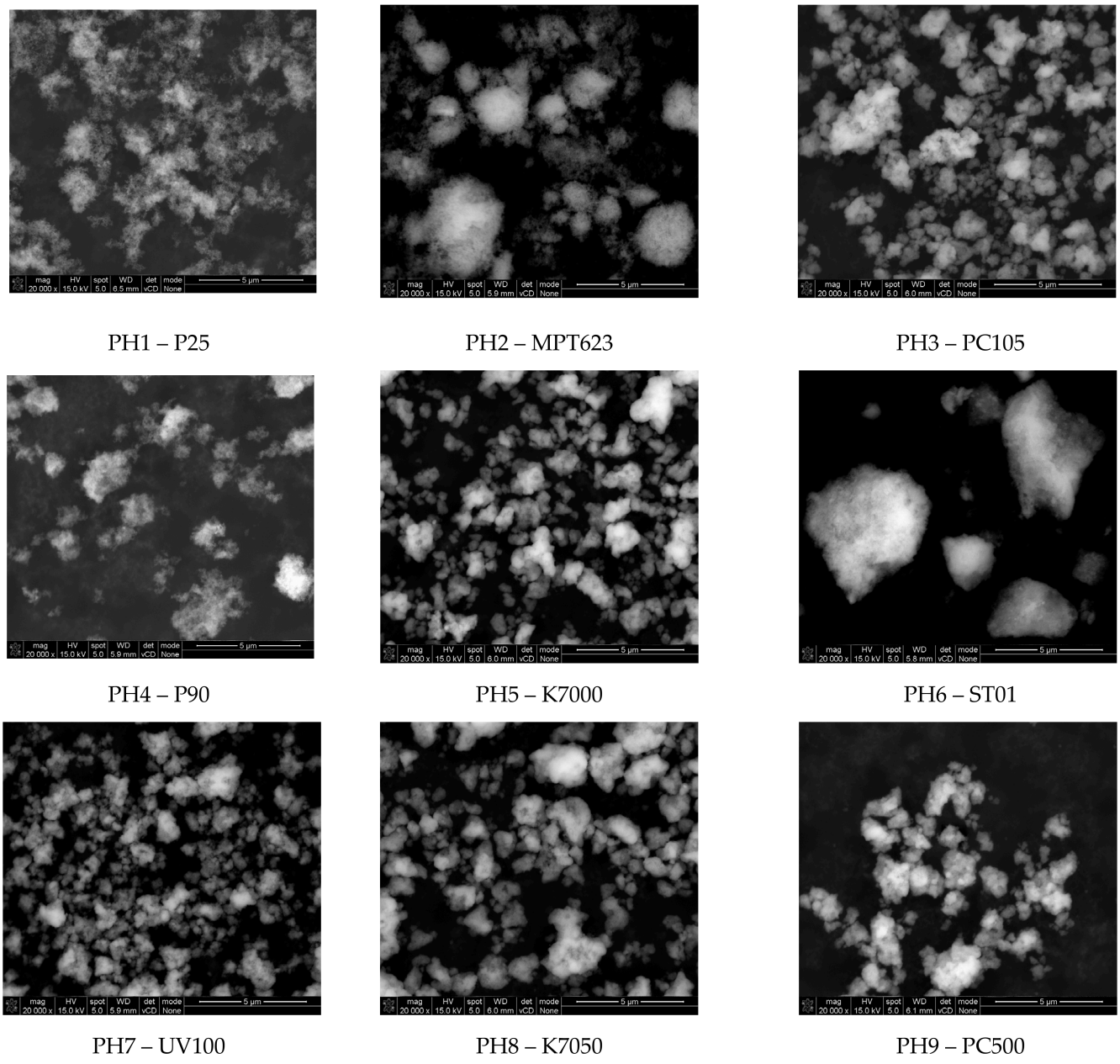


Figure 11. Representative SEM micrographs of the investigated photocatalyst powders.

Among the investigated photocatalysts, two materials have been specifically developed to exhibit visible-light photocatalytic activity: MPT623 and K7000. These photocatalysts employ fundamentally different modification strategies. MPT623 is a Pt-modified rutile TiO_2 photocatalyst, in which platinum species deposited on the particle surface enhance charge separation by acting as electron traps and reducing electron–hole recombination [30,31]. In contrast, K7000 is a carbon-modified anatase TiO_2 photocatalyst, in which carbon-containing species have been reported to alter the electronic structure and extend the photoresponse toward the visible region [32,33]. The remaining photocatalysts (P25, P90, PC105, ST01, UV100, and K7050) represent conventional TiO_2 materials whose photocatalytic performance is primarily governed by differences in phase composition, crystallite size, particle morphology, and specific surface area rather than by intentional chemical modification.

The investigated photocatalysts exhibited substantial differences in BET specific surface area, ranging from 53.8 m^2/g for P25 to 360.6 m^2/g for PC500. High specific surface areas

above 300 m^2/g were also observed for K7050, ST01, and UV100, whereas P25, P90, and MPT623 exhibited significantly lower BET values.

XRD analysis showed that most photocatalysts consisted predominantly or entirely of anatase. P25 and P90 contained mixed anatase–rutile phase compositions, with anatase contents of 87% and 91%, respectively. In contrast, MPT623 consisted entirely of rutile. The investigated materials also differed substantially in crystallite size. The smallest anatase crystallites (~8–10 nm) were observed for K7050, PC500, ST01, UV100, and K7000, while P25 and P90 exhibited noticeably larger crystallites.

UV–Vis analysis indicated relatively similar band-gap energies for most investigated photocatalysts, typically 3.25–3.33 eV, characteristic of conventional anatase TiO_2. A noticeably lower band-gap energy of 3.06 eV was observed for MPT623. This reduction is consistent with the presence of platinum species, which have been reported to introduce additional electronic states and facilitate visible-light absorption through enhanced charge-transfer processes [31]. In contrast, K7000, despite being a carbon-modified photocatalyst designed for visible-light applications, exhibited a band gap comparable to that of unmodified anatase materials. The investigated photocatalysts also differed in absorption maxima and absorbance intensities, indicating variations in optical response despite relatively similar TiO_2 contents as determined by XRF analysis [S4].

The SEM observations revealed substantial differences in agglomeration structure and particle morphology between the investigated photocatalysts, despite several materials exhibiting similar phase compositions and optical properties. High-BET nano-anatase photocatalysts such as K7000, K7050, UV100, and PC500 generally consisted of highly fragmented nanosized particles that formed dense secondary agglomerates, whereas P25 and P90 exhibited comparatively more open, loosely packed agglomerate structures despite their lower BET surface areas and larger crystallite sizes. ST01 was characterized by particularly large compact agglomerates, while the rutile-based MPT623 exhibited smoother and denser particle morphology.

4.1.2. Other Cement Mortar Constituents

Materials used for preparation of the photocatalytic mortars included Portland cement CEM I 42.5R (Cement Ożarów, Ożarów, Poland, compliant with PN-EN 197-1 [34]), Portland-slag cement CEM II/B-S 42.5R (Cement Ożarów, Ożarów, Poland, compliant with PN-EN 197-1 [34]), silica fume (MSILICA Tech, Łaziska Górne, Poland, compliant with PN-EN 13263-1 [35]), quartz powder (Orbud, Łódź, Poland, compliant with ISO/DIS 3262-13 [36]), natural quartz sand (Corrado Kruszywa, Łajski, Poland, compliant with PN-EN 13139 [37]), tap water (compliant with EN 1008 [38]), and a polycarboxylate ether-based superplasticizer (Master Builders Solutions, Myślenice, Poland, compliant with PN-EN 934-2 [39]). The blend of CEM I and CEM II/B-S cements was used to obtain a binder composition similar to that of CEM II/A-S, which is commonly used in precast concrete production. Two quartz sand fractions were used to improve particle packing and ensure a homogeneous mortar matrix. Silica fume and quartz powder were incorporated as supplementary microfillers to enhance matrix densification and limit excessive porosity development. The BET specific surface area of the silica fume was 2.59 m^2/g, while the specific surface area of the quartz powder determined using the laser diffraction method was 0.151 m^2/g. The superplasticizer was used to ensure adequate workability and facilitate homogeneous dispersion of the photocatalytic powders within the cementitious matrix.

The physicochemical characteristics of the applied binders and aggregates are summarized in Tables 3 and 4, while additional details are provided in previous studies [40–42].

Table 3. Selected properties of the cements used in the study. The properties were determined in accordance with PN-EN 196-1 [43] (mechanical properties), PN-EN 196-3 [44] (initial and final setting time), and PN-EN 196-6 [45] (specific surface area).

Type of Cement	Flexural Strength, 28 Days	Compressive Strength, 28 Days	Initial Setting Time	Final Setting Time	Specific Surface Area
	MPa	MPa	min	min	cm^2/g
CEM I 42.5R	4.5	44.4	190	270	3920
CEM II/B-S 42.5R	4.8	42.7	210	350	4830

Table 4. Selected properties of the aggregates used in the study in accordance with PN-EN 13139 [37].

Granulation	Dust Content	Water Absorption	SiO_2 Content	Fe_2O_3 Content	Al_2O_3 Content	Softening Point	Sulfur Content	Sand Equivalent
mm	%	%	%	%	%	°C	%	-
0.1/0.5	0.1	0.1	99.6	0.01	0.06	1506	<1	99.06
0.5/1.2	0.1	0.1	99.4	0.01	0.05	1582	<1	99.17

4.2. Methods

4.2.1. Photocatalytic Properties

The specific surface area was determined using the Brunauer–Emmett–Teller (BET) method with a Gemini VII 2390t analyzer (Micromeritics Instrument Corporation, Norcross, GA, USA). The measurements were performed using nine-point nitrogen adsorption–desorption isotherms over the relative pressure range of 0.05–0.25 p/p°.

Phase composition and crystallite size were determined by X-ray diffraction (XRD). The measurements were performed using a Bruker AXS D8 DAVINCI (Bruker AXS, Billerica, MA, USA) diffractometer operating in the Bragg–Brentano configuration and equipped with a Cu anode X-ray lamp (Cu Kα radiation). The diffraction patterns were recorded over the angular range 5–120° 2θ with a step size of 0.01° and a counting time of 2 s per step. The optical configuration consisted of a 0.3° divergence slit, a 1.5° anti-scatter slit, two 2.5° Soller slits, a Ni filter, and a LynxEye strip detector with a field of view of 2.94°. The total acquisition time for a single diffraction pattern was approximately 6 h 15 min. The samples were prepared as pressed powder specimens, additionally ground in an agate mortar prior to analysis. Phase identification was performed using the DIFFRACplus EVA-SEARCH (version 6) software and the COD crystallographic database. Quantitative phase analysis and crystallite size determination were carried out using the Rietveld refinement method implemented in TOPAS v5.0 based on crystallographic structures available in the COD database. Instrumental broadening was determined using a LaB6 reference material. The complete diffraction patterns together with the corresponding Rietveld refinement plots are provided in the Supplementary Materials [S1 and S2].

Chemical composition was determined using X-ray fluorescence spectroscopy (XRF) with an Axios Minerals spectrometer (Malvern Panalytical, Almelo, The Netherlands) equipped with a Rh anode X-ray lamp. Due to difficulties in preparing fused beads, the samples were analyzed as pressed-powder pellets. Chemical composition calculations were performed using the IQ+ method.

Morphology and microstructure were investigated using a field-emission scanning electron microscope (FE-SEM, Nova NanoSEM 200, FEI, Hillsboro, OR, USA). Backscattered electron imaging (BSE) was performed using a vCD detector, while elemental analysis was conducted using an Octane Elect energy-dispersive spectroscopy (EDS) detector (EDAX, Mahwah, NJ, USA).

Optical properties were evaluated using a V-670 UV–Vis–NIR spectrophotometer (Jasco, Tokyo, Japan) equipped with an ETCS-761 Peltier thermostatted single-position cell holder and an ISN-723 integrating sphere. The absorption spectra were used to determine the optical band-gap energies using the Tauc method after converting wavelength data to photon energy and appropriately transforming the absorption intensity. The complete UV–Vis absorption spectra are provided in the Supplementary Materials [S3].

Photocatalytic air-purification performance toward nitrogen oxides was evaluated using a procedure developed by the authors, based on ISO 22197-1 [19]. The experimental setup (Figure 12) consisted of a sealed glass reaction chamber equipped with a controlled gas-flow system and two irradiation sources. UV-A illumination was provided by LED strips (LuxaLight, Eindhoven, The Netherlands) with a peak wavelength of 365 ± 5 nm and a nominal power of 14.4 W/m. The global UV-A irradiance at the sample surface was adjusted to 1.0 W/m^2. Visible-light irradiation was provided by SunLike™ TRI-R™ LED strips (5000 K) (Seoul Semiconductor, Ansan, South Korea), with the global irradiance adjusted to 150 W/m^2. The irradiance levels were selected to simulate typical outdoor lighting conditions observed in Poland during the autumn–winter period. UV-A irradiance was measured using a Delta Ohm radiometer (Delta OHM S.r.l., Caselle di Selvazzano, Padova, Italy) covering the 315–400 nm wavelength range, whereas the global irradiance of visible light was measured using a Lambrecht METEO pyranometer operating within the spectral range of 285–3000 nm.

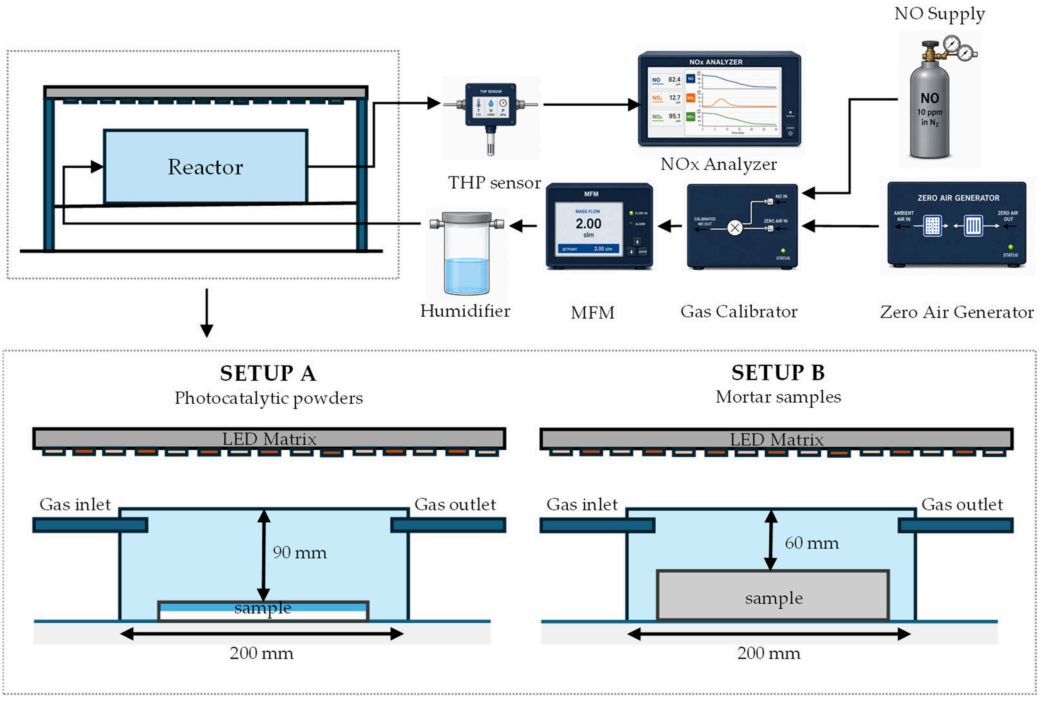


Figure 12. Experimental setup for evaluating the air-purification performance of photocatalytic powders (SETUP A) and cement mortar specimens (SETUP B) (THP—temperature–humidity–pressure sensor; MFM—mass flow meter). Both experimental configurations employed the same reactor geometry and gas inlet–outlet arrangement, with the specimen surface positioned 90 mm (SETUP A) or 60 mm (SETUP B) below the gas inlet–outlet level. The configuration remained unchanged within each experimental series.

During the experiments, the temperature inside the reaction chamber was maintained at 25 ± 5 °C. Owing to the hygroscopic nature of the investigated powders, the relative humidity was controlled at 20 ± 2% to minimize the influence of moisture adsorption on the measured photocatalytic performance. The gas flow rate was kept constant at

2 L/min. Nitric oxide concentrations were continuously monitored using a Teledyne API T200 chemiluminescence analyzer (Teledyne API, San Diego, CA, USA). The initial NO concentration was stabilized at 100 ± 5 ppb prior to irradiation in order to simulate typical urban atmospheric pollution levels.

For powder-scale experiments, 8 g of the investigated material was placed in a 145 mm Petri dish and manually compacted under gentle pressure to obtain a relatively uniform exposed surface. After stabilization of the inlet NO concentration, the UV-A irradiation was switched on and maintained for 40 min. The concentrations of NO, NO_2, and NOx were continuously recorded throughout the experiment. To eliminate the influence of lamp stabilization and transient concentration fluctuations immediately after illumination, the first 10 min of each irradiation phase were excluded from the calculations. The amounts of removed NO and generated NO_2 were determined by integrating the corresponding concentration–time curves over the remaining 30 min. The resulting integrated areas, schematically shown in Figure 13a, were converted to reaction rates (μg/(m²·h)).

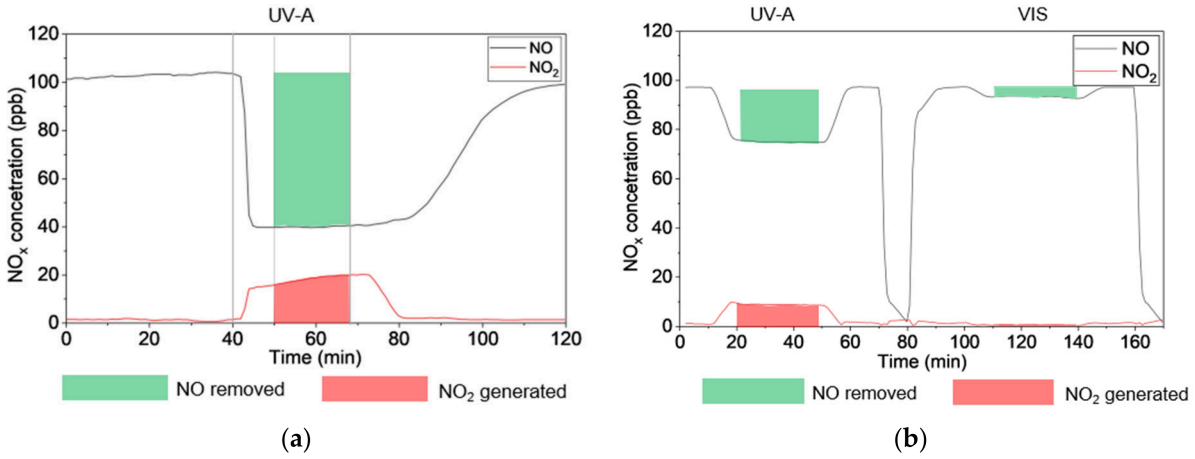


Figure 13. Representative NO concentration profiles of photocatalytic testing of (**a**) photocatalytic powders under UV-A irradiation (SETUP A) and (**b**) cement mortar specimens under sequential UV-A and visible-light irradiation (SETUP B). Each irradiation phase lasted 40 min, with the first 10 min excluded from the calculation of photocatalytic reaction rates.

Additionally, dynamic light scattering (DLS) and zeta potential measurements were performed under simulated cement pore-solution conditions to evaluate the effective particle size and colloidal stability in highly alkaline cementitious environments. The measurements were performed using a Zetasizer Nano ZS (Malvern Panalytical Ltd., Malvern, UK). Particle size distribution was determined using the DLS method based on intensity-weighted distributions, while zeta potential was determined by electrophoretic light scattering (ELS). The measurements were conducted at 25 °C using diluted suspensions prepared in a simulated cement pore solution.

4.2.2. Mortar Properties

The self-cleaning performance of the investigated mortars was evaluated using a rhodamine B discoloration test based on UNI 11259 [46]. A rhodamine B solution (0.1 g/L) was applied to the specimen surfaces as four droplets (0.5 mL each), which were then allowed to absorb in the dark for 24 h. The color changes induced by photocatalytic degradation of rhodamine were quantified using a spectrophotometer (NS810, Shenzhen 3nh Technology Co., Ltd., Shenzhen, China) operating in the CIELab* color space. For each rhodamine spot, three measurements were performed and averaged, yielding 12 measurements per specimen.

After the initial measurement, the specimens were exposed to UV-A irradiation at 4 W/m^2, in accordance with UNI 11259 [46]. The self-cleaning efficiency was assessed by measuring the reduction in the a* parameter, which represents the red-green color coordinate and is directly related to rhodamine staining intensity. The self-cleaning indicators after 24 h (R24) of irradiation were calculated in accordance with UNI 11259 [46]. A detailed description of the test procedure and data processing methodology can be found in a previous study [42].

The photocatalytic NOx abatement performance of the cement mortar specimens was evaluated using the same experimental setup, gas composition, relative humidity, and irradiation conditions. The specimens measured 160 × 140 × 40 mm and were placed directly inside the reaction chamber.

Prior to testing, the specimens underwent a standardized surface preparation procedure. First, they were irradiated with UV-A light (10 W/m^2) for 24 h to remove residual organic contaminants from sample preparation and handling. Subsequently, the surfaces were rinsed with water, gently scrubbed, and dried at 105 °C for 24 h. All mortar specimens underwent identical pretreatment conditions, while their compositions differed only in photocatalyst type and dosage, thereby limiting the influence of specimen preparation and initial moisture conditions on comparative NOx abatement measurements.

Unlike the powder tests, which were conducted exclusively under UV-A irradiation, mortar specimens were exposed sequentially to two irradiation conditions: UV-A and visible light. Each irradiation phase lasted 40 min comprising an initial 10-min stabilization period followed by 30 min of data integration. The amounts of NO removed and NO_2 generated were calculated using the same procedure as for the powder photocatalysts and expressed as reaction rates in $\mu g/(m^2 \cdot h)$ (Figure 13b).

4.2.3. Mortar Specimen Preparation and Curing Conditions

The mortars were prepared in accordance with PN-EN 196-1 [43], with minor modifications to improve the dispersion of the photocatalytic powders. Water and the initial portion of the superplasticizer were first placed in the mixing bowl, followed by cement, photocatalyst, silica fume, and quartz powder. The low-speed mixing stage and sand addition were performed in accordance with PN-EN 196-1 [43]. After the standard homogenization interval, the high-speed mixing stage was extended to 3 min to improve the mixture's homogeneity.

The consistency of the fresh mortar was evaluated using a free-flow test performed with the cone mold specified in PN-EN 1015-3 [47] (height: 60 mm, upper diameter: 70 mm, lower diameter: 100 mm). The target flow diameter was 180–220 mm. If the flow diameter was below this range, the remaining superplasticizer was added, and the mixture was mixed for an additional 1 min at high speed. Mixtures exhibiting excessive flow were discarded.

The mortars were cast into molds measuring 160 × 140 × 40 mm and compacted on a vibrating table for 2–3 s. The molds were covered with polyethylene foil and stored for 24 h. After demolding, the specimens were cured for 27 days in a climatic chamber maintained at 20 ± 2 °C and relative humidity above 95% prior to testing.

5. Experimental Framework

The experimental program was divided into two stages. In the first stage, the physicochemical properties of nine commercially available photocatalysts were characterized using XRD, XRF, BET, UV–Vis, and SEM/EDS. In parallel, the photocatalytic air purification performance of the powders was evaluated using NOx abatement tests.

Based on the results obtained in the first stage, seven representative photocatalysts were selected for further investigation in cementitious composites. In the second stage, these

photocatalysts were incorporated into a high-performance mortar specifically designed for photocatalytic applications, such as the surface layer of precast concrete elements. The composition of the reference mortar is presented in Table 5. The photocatalytic performance of the mortars was evaluated through NOx abatement tests. Subsequently, six photocatalysts were selected for self-cleaning investigations to provide a representative range of NOx-abatement behaviors while limiting experimental redundancy. One material showing a photocatalytic response closely comparable to another selected photocatalyst was therefore omitted from this stage.

Table 5. The composition of the reference mortar of water-to-binder ratio 0.34.

CEM I 42.5 R	CEM II B/S 42.5 R	Silica Fume	Quartz Powder	Water	PCE Superplasticizer	Quartz Sand	
						0.1/0.5	0.5/1.2
kg/m^3							
566	241	10	113	279	3.14	519	519

The experimental design considered two independent variables: photocatalyst type and photocatalyst dosage. Eight dosage levels were investigated: 4, 6, 8, 10, 12, 14, 16, and 18 kg per m^3 of mortar. The overall experimental framework is presented schematically in Figure 14.

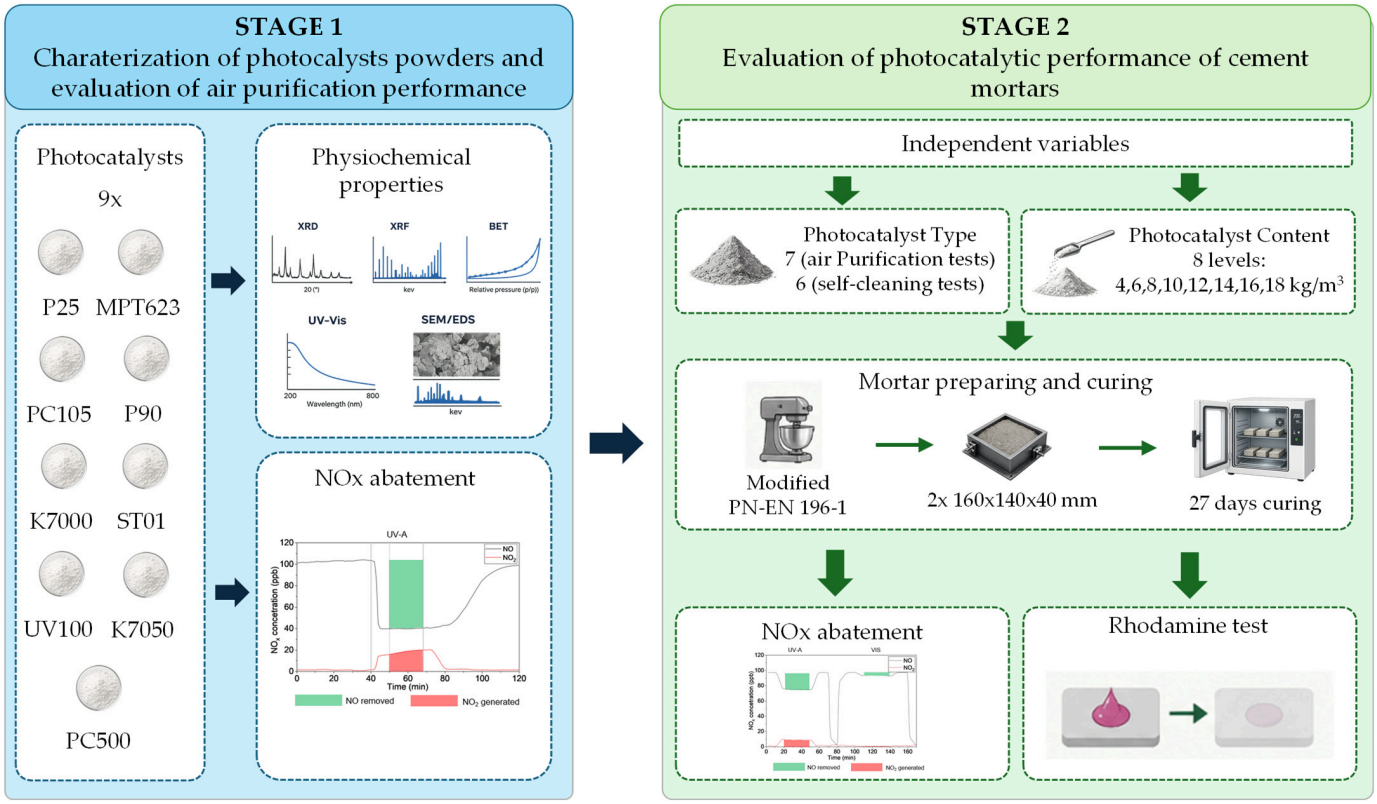


Figure 14. Experimental framework.

6. Conclusions

This study tested the central hypothesis that the physicochemical properties governing the intrinsic activity of TiO_2 powders are not necessarily the properties that determine their effectiveness after incorporation into a cementitious matrix. Nine commercial photocatalysts spanning a wide range of phase compositions, crystallite sizes, BET surface areas, and optical characteristics were first examined as powders, after which seven representative materials

were incorporated into cementitious mortar at dosages of 4–18 kg/m^3. The results supported the proposed hypothesis and identified photocatalyst accessibility after hydration, rather than nominal powder activity alone, as the critical link between material characteristics and composite-scale performance. The principal findings are as follows:

- The investigated photocatalytic powders were characterized by BET surface areas ranging from 53.8 to 360.6 m^2/g and NO removal rates from 357 to 561 μg/(m^2·h). Powder-scale NO removal correlated positively with BET surface area and anatase content. Moreover, the increase in activity became progressively smaller above approximately 200–240 m^2/g, demonstrating that the beneficial effect of increasing BET surface area is not unlimited.
- Powder-scale NO removal did not fully describe the environmental utility of the photocatalysts as the extent of NO_2 formation differed substantially. PC500 achieved the highest NO removal (approximately 561 μg/(m^2·h)) but also generated approximately 257 μg/(m^2·h) of NO_2, with the lowest selectivity (0.70). In contrast, K7000 combined relatively high NO removal with a selectivity of 0.96. Photocatalyst evaluation should therefore consider net NOx removal and reaction selectivity rather than gross NO conversion alone.
- Incorporation into cement mortar fundamentally changed the photocatalytic performance of the modifiers established from the powder tests. P25, which had the lowest powder-scale NO removal and the lowest BET surface area, produced the highest mortar-scale activity, reaching approximately 220 μg/(m^2·h) NO removal at 18 kg/m^3. It also exhibited the highest self-cleaning efficiency. Conversely, the high-BET photocatalysts K7000, UV100, K7050, and ST01 generally remained below 80 μg/(m^2·h), even at the highest dosages. The best-performing powder was therefore not necessarily the most effective photocatalyst after immobilization within the cement matrix.
- A novel framework based on two complementary indicators, the Photocatalytic Utility Index (PUI) and the Dose–Response Index (DRI), was proposed to quantify the transfer of powder-level photocatalytic performance to cementitious composites and its response to increasing photocatalyst content. The low-BET photocatalysts exhibited PUI values of approximately 0.16–0.24, compared with only 0.01–0.06 for the high-BET group. P90 showed the highest PUI (0.238), whereas P25 exhibited the highest DRI (0.448), followed by MPT623 (0.322) and P90 (0.154). In contrast, DRI values for the high-BET photocatalysts ranged from approximately 0 to 0.098, indicating both lower overall utilization of powder-level performance and a weaker response to increasing photocatalyst content under the conditions investigated. The complementary PUI and DRI descriptors were further proposed as a basis for an application-specific utility index (U), in which their relative contributions can be weighted according to the performance requirements of a given cementitious application.
- The limited transfer of high-BET powder activity was not explained by agglomerate size alone. All photocatalysts formed micrometer-sized agglomerates of approximately 1.9–7.4 μm in simulated cement pore solution, while zeta potentials between approximately −4 and +3 mV indicated very low colloidal stability. The high-BET materials, composed predominantly of crystallites approximately 8–10 nm in size, provided a substantially greater interfacial area for heterogeneous nucleation than the lower-BET photocatalysts with crystallites approximately 18–33 nm in size. This promoted the formation of hydration products on and around the TiO_2 agglomerates, progressively restricting their exposure to incident radiation and gaseous reactants. SEM/EDS observations provided direct microstructural visualizations consistent with this mechanism. P25 formed Ti-rich agglomerates of approximately 7–7.5 μm, matching the DLS results, and a proportion of these agglomerates protruded above the surrounding cement

matrix. In contrast, the Ti-rich regions identified in the K7000-containing mortar were predominantly covered by Ca- and Si-rich hydration products.

- Photocatalytic performance remained dependent on the target reaction and irradiation conditions. MPT623 was the only material to retain a pronounced visible-light response, reaching an NO removal rate of approximately 64 $\mu g/(m^2 \cdot h)$ at 18 kg/m^3, whereas K7000 did not exhibit significant visible-light NO removal despite being marketed as visible-light active. At the same time, K7000 reached an R24 value of approximately 0.78 in the Rhodamine B test, comparable to MPT623 (R24 = 0.79) and P90 (R24 = 0.76), despite its limited gas-phase NOx removal. Gas-phase pollutant abatement and dye discoloration, therefore, probe different aspects of photocatalytic performance and should be treated as complementary rather than interchangeable evaluation methods.

Collectively, the results demonstrate that photocatalyst selection for cementitious composites cannot be reduced to maximizing BET surface area, minimizing crystallite size, or identifying the most active powder. Effective design requires simultaneous consideration of powder-level photocatalytic performance, NOx oxidation selectivity, dose responsiveness, agglomeration under alkaline conditions, interactions with hydration products, and the preservation of an exposed photocatalyst population at the composite surface. Powder characterization should therefore be complemented by composite-scale testing under the intended incorporation method, matrix composition, curing regime, irradiation conditions, and target application. Accordingly, the most active photocatalyst powder is not necessarily the most effective photocatalyst for a cementitious material.

Supplementary Materials: The following supporting information can be downloaded at https://www.mdpi.com/article/10.3390/catal16111029/s1, S1: XRD; S2: Rietveld; S3: UV-VIS; S4: XRF.

Author Contributions: Conceptualization, W.J.-R., K.C. and M.K.; methodology, W.J.-R., K.C., M.K., B.J. and F.C.; software, K.C. and M.K.; validation, W.J.-R., M.K. and K.C.; formal analysis, W.J.-R., M.K. and K.C.; investigation, W.J.-R., K.C., M.K., B.J. and F.C.; resources, W.J.-R., M.K. and K.C.; data curation, M.K. and K.C.; writing—original draft preparation, K.C., M.K. and W.J.-R.; writing—review and editing, W.J.-R., K.C., M.K., B.J. and F.C.; visualization, M.K. and K.C.; supervision, W.J.-R.; project administration, W.J.-R., M.K. and K.C.; funding acquisition, M.K. All authors have read and agreed to the published version of the manuscript.

Funding: This research received support under a 2026 research grant from the Warsaw University of Technology, supporting scientific activity in the discipline of Civil Engineering, Geodesy, and Transport.

Data Availability Statement: The data are included in the paper and are available on request.

Conflicts of Interest: The authors declare no conflicts of interest.

References

1. Ballari, M.M.; Yu, Q.L.; Brouwers, H.J.H. Experimental study of the NO and NO2 degradation by photocatalytically active concrete. *Catal. Today* **2011**, *161*, 175–180. [CrossRef]
2. Jimenez-Relinque, E.; Rodriguez-Garcia, J.R.; Castillo, A.; Castellote, M. Characteristics and Efficiency of Photocatalytic Cementitious Materials: Type of Binder, Roughness and Microstructure. *Cem. Concr. Res.* **2015**, *71*, 124–131. [CrossRef]
3. Fei, H.; Wu, J.; Zhang, J.; Zhao, T.; Guo, W.; Wang, X.; Yang, S.; Liu, G. Photocatalytic Performance and Its Internal Relationship with Hydration and Carbonation of Photocatalytic Concrete: A Review. *J. Build. Eng.* **2024**, *97*, 110782. [CrossRef]
4. Chen, C.; Tang, B.; Cao, X.; Gu, F.; Huang, W. Enhanced Photocatalytic Decomposition of NO on Portland Cement Concrete Pavement Using Nano-TiO2 Suspension. *Constr. Build. Mater.* **2021**, *275*, 122135. [CrossRef]
5. Staub de Melo, J.V.; Trichês, G. Evaluation of the Influence of Environmental Conditions on the Efficiency of Photocatalytic Coatings in the Degradation of Nitrogen Oxides (NOx). *Build. Environ.* **2012**, *49*, 117–123. [CrossRef]
6. Yu, Q.L.; Brouwers, H.J.H. Indoor Air Purification Using Heterogeneous Photocatalytic Oxidation. Part I: Experimental Study. *Appl. Catal. B Environ.* **2009**, *92*, 454–461. [CrossRef]

7. Seo, D.; Yun, T.S. NOx Removal Rate of Photocatalytic Cementitious Materials with TiO2 in Wet Condition. *Build. Environ.* **2017**, *112*, 233–240. [CrossRef]
8. Wang, H.; Wu, Z.; Zhao, W.; Guan, B. Photocatalytic Oxidation of Nitrogen Oxides Using TiO2 Loading on Woven Glass Fabric. *Chemosphere* **2007**, *66*, 185–190. [CrossRef] [PubMed]
9. Ahmad, R.; Ahmad, Z.; Khan, A.U.; Mastoi, N.R.; Aslam, M.; Kim, J. Photocatalytic Systems as an Advanced Environmental Remediation: Recent Developments, Limitations and New Avenues for Applications. *J. Environ. Chem. Eng.* **2016**, *4*, 4143–4164. [CrossRef]
10. Guo, M.-Z.; Maury-Ramirez, A.; Poon, C.S. Self-Cleaning Ability of Titanium Dioxide Clear Paint Coated Architectural Mortar and Its Potential in Field Application. *J. Clean. Prod.* **2016**, *112*, 3583–3588. [CrossRef]
11. Kalinowski, M.; Chilmon, K.; Jackiewicz-Rek, W. Photocatalytic Performance of Cementitious Composites Modified with Second-Generation Nano-TiO2 Dispersions: Influence of Composition and Granulation on NOx Purification Efficiency. *Coatings* **2025**, *15*, 148. [CrossRef]
12. Witkowski, H.; Jarosławski, J.; Szkop, A.; Chilmon, K.; Kalinowski, M.; Jackiewicz-Rek, W. The Potential Risk of Nanopartic-ulate Release from Photocatalytic Pavement Concrete Surface Due to a Simulated Abrasion Load—An Experimental Study. *Materials* **2024**, *17*, 3022. [CrossRef] [PubMed]
13. Pinho, L.; Mosquera, M.J. Photocatalytic activity of TiO2–SiO2 nanocomposites applied to buildings: Influence of particle size and loading. *Appl. Catal. B Environ.* **2013**, *134*, 205–221. [CrossRef]
14. Valeeva, A.A.; Sushnikova, A.A.; Rempel, A.A. Phase composition tuning by high-energy ball milling of titanium dioxide powders. *Inorg. Chem. Commun.* **2024**, *159*, 111727. [CrossRef]
15. Folli, A.; Pade, C.; Hansen, T.B.; De Marco, T.; Macphee, D.E. TiO2 Photocatalysis in Cementitious Systems: Insights into Self-Cleaning and Depollution Chemistry. *Cem. Concr. Res.* **2012**, *42*, 539–548. [CrossRef]
16. Akbulut, Z.F. Influence of Nano-TiO2 Particle Size on Fresh, Physical, Mechanical, Photocatalytic, and Cost Performance of Cement Mortars. *ACS Omega* **2026**, *11*, 24835–24850. [CrossRef] [PubMed]
17. Naniwa, S.; Kato, K.; Yamakata, A.; Yamamoto, A.; Yoshida, H. A Quantitative Study on the Relationship of Specific Surface Area and Carrier Lifetime to Photocatalytic Activity of Anatase TiO2 Nanoparticles. *ACS Catal.* **2023**, *13*, 15212–15218. [CrossRef]
18. Nandal, V.; Seki, K. General Size Effects versus Specific Surface Reactivity in Particulate Photocatalyst Efficiency. *J. Phys. Chem. C* **2026**, *130*, 1081–1087. [CrossRef]
19. *ISO 22197-1:2016*; Fine Ceramics (Advanced Ceramics, Advanced Technical Ceramics)—Test Method for Air-Purification Performance of Semiconducting Photocatalytic Materials—Part 1: Removal of Nitric Oxide. International Organization for Standardization: Geneva, Switzerland, 2016.
20. Chen, J.; Poon, C.-S. Photocatalytic Cementitious Materials: Influence of the Microstructure of Cement Paste on Photocatalytic Pollution Degradation. *Environ. Sci. Technol.* **2009**, *43*, 8948–8952. [CrossRef] [PubMed]
21. Folli, A.; Pochard, I.; Nonat, A.; Jakobsen, U.H.; Shepherd, A.M.; Macphee, D.E. Engineering Photocatalytic Cements: Understanding TiO2 Surface Chemistry to Control and Modulate Photocatalytic Performances. *J. Am. Ceram. Soc.* **2010**, *93*, 3360–3369. [CrossRef]
22. Baudys, M.; Berthet, E.; Macak, J.M.; Lhotka, M.; Krýsa, J. Photocatalytic Degradation of Gaseous Pollutants on Nanostructured TiO2 Films of Various Thickness and Surface Area. *Photochem. Photobiol. Sci.* **2023**, *22*, 883–892. [CrossRef] [PubMed]
23. Hamidi, F.; Aslani, F. TiO2-Based Photocatalytic Cementitious Composites: Materials, Properties, Influential Parameters, and Assessment Techniques. *Nanomaterials* **2019**, *9*, 1444. [CrossRef] [PubMed]
24. Guo, M.-Z.; Ling, T.-C.; Poon, C.S. Photocatalytic NOx Degradation of Concrete Surface Layers Intermixed and Spray-Coated with Nano-TiO2: Influence of Experimental Factors. *Cem. Concr. Compos.* **2017**, *83*, 279–289. [CrossRef]
25. Si, H.; Zhou, M.; Fang, Y.; He, J.; Yang, L.; Wang, F. Photocatalytic Concrete for NOx Degradation: Influence Factors and Durability. *Constr. Build. Mater.* **2021**, *298*, 123835. [CrossRef]
26. Casagrande, C.A.; Repette, W.L.; Hotza, D. Effect of Environmental Conditions on Degradation of NOx Gases by Photocatalytic Nanotitania-Based Cement Mortars after Long-Term Hydration. *J. Clean. Prod.* **2020**, *274*, 123067. [CrossRef]
27. Ha, S.; Min, C.G.; Lee, I.W.; Chae, E.; Lim, C.; Lee, Y.-S. High-Efficiency Photocatalyst C@TiO2 with the Synergy Effect of Carbon Doping and Phase Transformation. *Mater. Today Chem.* **2024**, *42*, 102385. [CrossRef]
28. Yu, S.; Yun, H.J.; Kim, Y.H.; Yi, J. Carbon-Doped TiO2 Nanoparticles Wrapped with Nanographene as a High Performance Photocatalyst for Phenol Degradation under Visible Light Irradiation. *Appl. Catal. B Environ.* **2014**, *144*, 893–899. [CrossRef]
29. Abreu-Jaureguí, C.; Andronic, L.; Sepúlveda-Escribano, A.; Silvestre-Albero, J. Improved Photocatalytic Performance of TiO2/Carbon Photocatalysts: Role of Carbon Additive. *Environ. Res.* **2024**, *251*, 118672. [CrossRef] [PubMed]
30. Doss, N.; Carré, G.; Keller, V.; André, P.; Keller, N. Photocatalytic Decontamination of Airborne T2 Bacteriophage Viruses in a Small-Size TiO2/β-SiC Alveolar Foam LED Reactor. *Water Air Soil Pollut.* **2018**, *229*, 29. [CrossRef]
31. Doss, N.; Bernhardt, P.; Romero, T.; Masson, R.; Keller, V.; Keller, N. Photocatalytic Degradation of Butanone (Methylethyl-ketone) in a Small-Size TiO2/β-SiC Alveolar Foam LED Reactor. *Appl. Catal. B Environ.* **2014**, *154–155*, 301–308. [CrossRef]

32. Arimi, A.; Dillert, R.; Dräger, G.; Bahnemann, D.W. Light-Induced Reactions of Chlorpromazine in the Presence of a Heterogeneous Photocatalyst: Formation of a Long-Lasting Sulfoxide. *Catalysts* **2019**, *9*, 627. [CrossRef]
33. Arimi, A.; Günnemann, C.; Curti, M.; Bahnemann, D.W. Regarding the Nature of Charge Carriers Formed by UV or Visible Light Excitation of Carbon-Modified Titanium Dioxide. *Catalysts* **2019**, *9*, 697. [CrossRef]
34. *PN-EN 197-1:2011*; Cement—Part 1: Composition, Specifications and Conformity Criteria for Common Cements. Polish Committee for Standardization: Warsaw, Poland, 2011.
35. *PN-EN 13263-1*; Silica Fume for Concrete—Part 1: Definitions, Requirements and Conformity Criteria. Polish Committee for Standardization: Warsaw, Poland, 2009.
36. *ISO 3262-13:1997*; Extenders—Specifications and Methods of Test—Part 13: Natural Quartz. International Organization for Standardization: Geneva, Switzerland, 1997.
37. *PN-EN 13139:2002*; Aggregates for Mortar. Polish Committee for Standardization: Warsaw, Poland, 2002.
38. *PN-EN 1008:2002*; Mixing Water for Concrete—Specification for Sampling, Testing and Assessing the Suitability of Water, Including Water Recovered from Processes in the Concrete Industry, as Mixing Water for Concrete. Polish Committee for Standardization: Warsaw, Poland, 2002.
39. *PN-EN 934-2:2009+A1:2012*; Admixtures for Concrete, Mortar and Grout—Part 2: Concrete Admixtures—Definitions, Requirements, Conformity, Marking and Labelling. Polish Committee for Standardization: Warsaw, Poland, 2012.
40. Chilmon, K.; Kalinowski, M.; Jackiewicz-Rek, W. Effect of Cement Substitution with Mineral Fillers on NOx Air-Purification Efficiency and Photocatalytic Reaction Selectivity of Nano-TiO2-Modified Cementitious Composites. *Materials* **2024**, *17*, 5775. [CrossRef] [PubMed]
41. Chilmon, K.; Kalinowski, M.; Jackiewicz-Rek, W. Influence of Coarse Aggregate Exposure on Air Purification Efficiency in Photocatalytic Cement Composites. *Buildings* **2024**, *14*, 3639. [CrossRef]
42. Kalinowski, M.; Chilmon, K.; Jackiewicz-Rek, W.; Rakowski, B. The Influence of Selected Material Variables of Photocatalytic Cementitious Composites on the Self-Cleaning Properties and Air Purification Efficiency from NOx Pollutants. *Sustainability* **2023**, *15*, 853. [CrossRef]
43. *PN-EN 196-1:2016-07*; Methods of Testing Cement—Part 1: Determination of Strength. Polish Committee for Standardization: Warsaw, Poland, 2016.
44. *PN-EN 196-3:2016*; Methods of Testing Cement—Part 3: Determination of Setting Times and Soundness. Polish Committee for Standardization: Warsaw, Poland, 2016.
45. *PN-EN 196-6:2019*; Methods of Testing Cement—Part 6: Determination of Fineness. Polish Committee for Standardization: Warsaw, Poland, 2019.
46. *UNI 11259:2016*; Photocatalysis—Determination of the Photocatalytic Activity of Hydraulic Binders—Rhodamine Test Method. Ente Nazionale Italiano di Unificazione (UNI): Rome, Italy, 2016.
47. *PN-EN 1015-3:2000*; Methods of Test for Mortar for Masonry—Part 3: Determination of Consistence of Fresh Mortar (by Flow Table). Polish Committee for Standardization: Warsaw, Poland, 2000.

Disclaimer/Publisher's Note: The statements, opinions and data contained in all publications are solely those of the individual author(s) and contributor(s) and not of MDPI and/or the editor(s). MDPI and/or the editor(s) disclaim responsibility for any injury to people or property resulting from any ideas, methods, instructions or products referred to in the content.